Simultaneous estimation of submerged floating tunnel displacement and mooring cable tension through FIR filter based strain and acceleration fusion

Zhanxiong Ma, Jaemook Choi, Jinho Jang, Ohjun Kwon and Hoon Sohn[*]

Department of Civil and Environmental Engineering, Korea Advanced Institute of Science and Technology, Daejeon, South Korea

Email: hoonsohn@kaist.ac.kr

Abstract: A submerged floating tunnel (SFT) is a tunnel structure that floats approximately 50 m below the water surface and is anchored to the seabed by mooring cables. It is a new alternative to conventional bridges and immersed tunnels. There have been ongoing efforts to construct SFTs worldwide, and the integrity of these SFTs need to be monitored throughout their lifespan. This study simultaneously estimated the tunnel displacement and mooring cable tension force using acceleration and strain measurements to assess the integrity of an SFT. First, strain measurements were transformed to displacement using simplified mode shapes and mode-scaling factors, which did not require the true mode shapes of the SFT. The mode-scaling factors were automatically estimated using initial strain and acceleration measurements. Then, the strain-based displacement was combined with the acceleration measurement using a finite impulse response filter to improve the displacement estimation accuracy. In addition, the tension force of a mooring cable was estimated from the displacement at the connection between the tunnel and mooring cable. The feasibility of the proposed technique was examined through a series of numerical simulations and laboratory tests on an 8-m-long aluminum SFT mock-up structure.

Keywords: Displacement estimation, tension force estimation, submerged floating tunnel, finite impulse response filter, strain gauge, accelerometer

1. Introduction

A submerged floating tunnel (SFT) is a tunnel structure floating approximately 50 m below the water surface and anchored to the seabed by mooring cables, as shown in Figure 1. The SFT is an attractive alternative to conventional bridges or immersed tunnels because its construction is not limited by the span length or depth of the ocean floor [1]. So far, no real-world SFT has been constructed, but there are ongoing efforts to build SFTs [2–5]. The development of monitoring systems to continuously evaluate the integrity of these SFTs is necessary. In particular, the measurements of the tunnel displacement and mooring cable tension force are critical for the structural integrity assessment of an SFT.

Several techniques are available for direct displacement measurements, utilizing linear variable differential transformers (LVDT) [6], real-time kinematic global navigation satellite systems (RTK-

GNSS) [7], vision-based systems [8], and radar systems [9,10]. Indirect displacement estimation techniques using accelerometers, inclinometer, and strain sensors have been developed recently as well [11–13]. Another trend for structural displacement estimation involves combining multiple types of measurements to improve the displacement measurement accuracy and reliability. Examples include combining RTK-GNSS and accelerometer [14], strain gauge and accelerometer [15,16], vision camera and accelerometer [17,18], and millimeter-wave radar and accelerometer [19]. Obviously, GNSS, radar, and vision-based techniques cannot operate in underwater environments, and the fusion of strain gauges and accelerometers seems to be promising for SFT displacement monitoring.
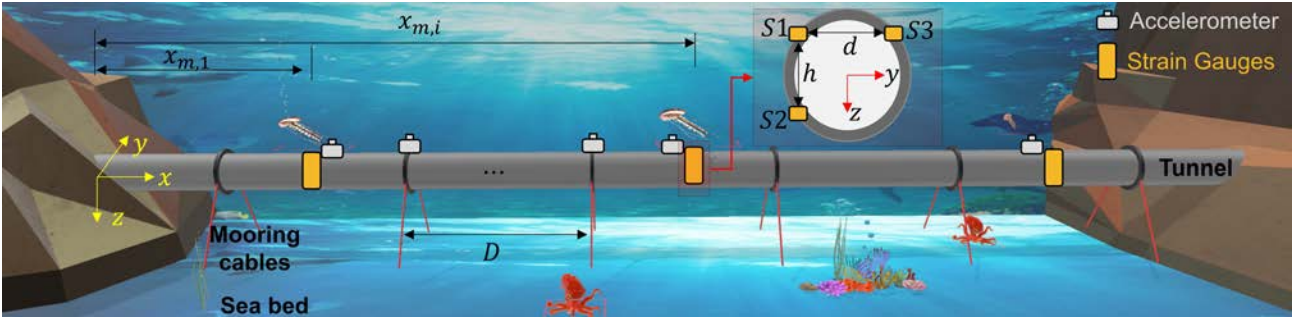

Figure 1. A conceptual sketch of a submerged floating tunnel (SFT) anchored to the seabed by mooring cables and sensor configuration of the proposed technique.

In addition to displacement, monitoring of the mooring cable tension force is also essential because mooring cables are major load-carrying members. Several cable tension force estimation techniques have been proposed, utilizing load cells [20], strain gauges [21], accelerometers [22,23], electromagnetic (EM) sensors [24,25], and eddy current sensors [26]. However, all of these discrete sensors must be physically placed on each cable, and such an installation can be time-consuming and labor-intensive. Although several attempts have been made to develop computer-vision techniques for noncontact tension force estimation [27,28], vision techniques cannot work in underwater environments.
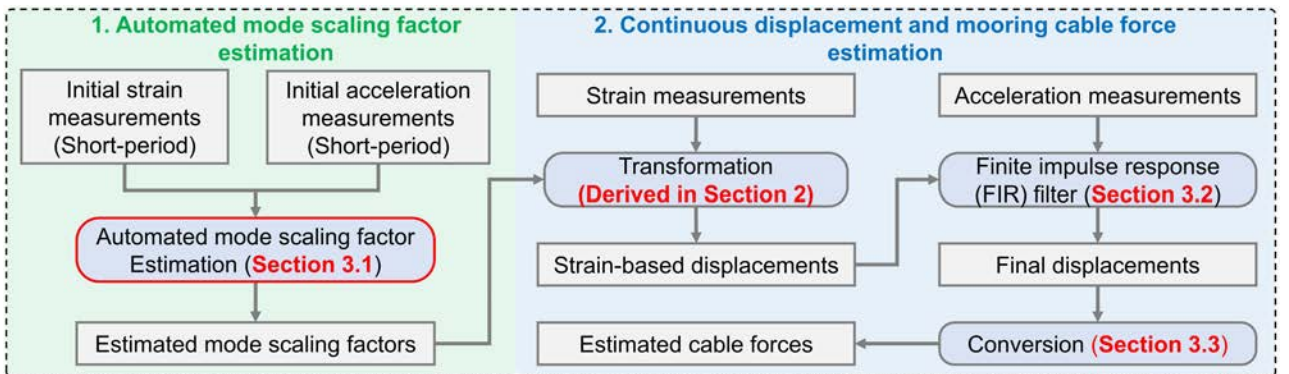

Figure 2. Flowchart of the proposed technique for simultaneous estimation of tunnel displacement and mooring cable tension using acceleration and strain measurements

This study simultaneously estimates the tunnel displacement and mooring cable tension force using acceleration and strain measurements. The sensor configuration for the proposed technique is shown in Figure 1. Strain gauges are installed at the mid-span locations of each tunnel segment ($x = x_{m,i}, i = 1, \cdots, N$), and bidirectional accelerometers are installed at locations where the displacement needs to be estimated. Figure 2 shows the flowchart of the proposed technique. First, the unknown mode-scaling factors necessary for the strain-displacement transformation (derived in Section 2) are estimated using the initial strain and acceleration measurements (less than 1 min) (Section 3.1). Second, the strain measurements after the first step are transformed to strain-based displacement using the derived transformation equation and estimated mode-scaling factors. Third, a finite impulse response (FIR) filter combines the strain-based displacement with acceleration measurements to improve displacement estimation accuracy (Section 3.2). Finally, the tension force of the mooring cable is estimated using the displacement estimated at the connection point of the mooring cable with the tunnel (Section 3.3). The performance of the proposed technique is examined in Section 4 through a series of numerical simulations, and in Section 5, a laboratory test on an 8-m-long aluminum SFT mock-up structure is presented. Concluding remarks are provided in Section 6. Note that no real-world SFT construction has been realized, an SFT structure form commonly used in previous studies [1-3] (as shown in Figure 1) is adopted in this study.

This study has the following contributions: (1) the displacement of an SFT is estimated by combining strain and acceleration measurements without knowing the true mode shapes of the SFT; (2) the tension force of a mooring cable is also estimated from the displacement at the connection point between the tunnel and the cable; and (3) the proposed displacement and tension force estimation technique is experimentally validated on an 8-m-long aluminum SFT structure.

2. Derivation of strain-displacement transformation relationship for SFTs with simplified mode shapes

2.1 Simplified model of SFTs

Previous studies have shown that an SFT can be simplified as a simple beam on an elastic foundation if the stiffness ratio is less than 0.05 [29]:

$$\frac{KD_x^3}{24EI} < 0.05 \tag{1}$$

where K denotes the axial stiffness of the mooring cables, D_x is the distance between two adjacent mooring cables in the x direction, and EI denotes the bending stiffness of the tunnel. When Equation (1) is satisfied, the displacement mode shapes of a simply supported beam (SSB) ($\bar{\psi}_j(x)$), hereafter referred to as the simplified displacement mode shapes, can approximate the true displacement mode shapes of an SFT ($\psi_j(x)$). Here, subscript j denotes the jth mode. These simplified displacement

mode shapes have been commonly used to analyze the dynamic responses of an SFT under seismic, vehicle, and impact loadings [30–32].
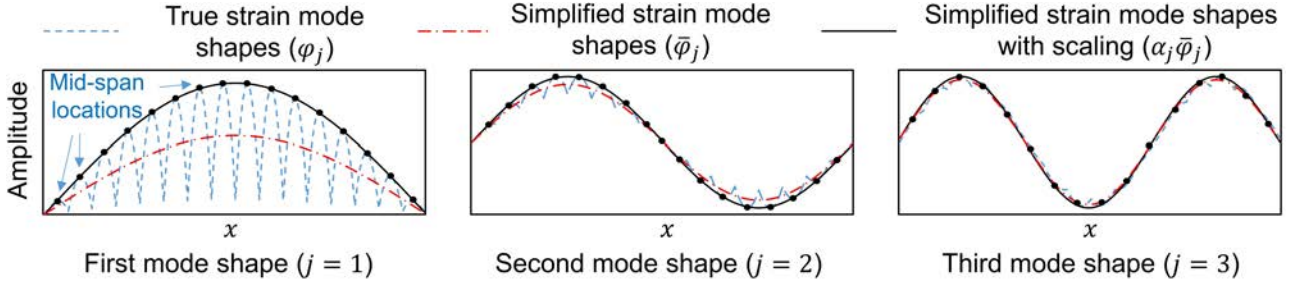

Figure 3. Comparison of the true and simplified strain mode shapes of an SFT

In practice, it is difficult to measure the structural displacement, especially in underwater environments. To tackle this issue, the strain is measured and transformed to displacement using a strain-displacement transformation relationship, which requires the strain mode shapes. Figure 3 shows the differences between the strain mode shapes of the SSB ($\bar{\varphi}_j(x)$) and the SFT ($\varphi_j(x)$). However, if only the strain mode shapes at the mid-span locations are of interest ($\varphi_j(x)$ at $x_{m,1}$, $x_{m,2}, \ldots x_{m,N}$), $\varphi_j(x)$ can be easily approximated by scaling $\bar{\varphi}_j(x)$ with a mode-scaling factor α_j. Note that as the mode order increases, the differences between $\bar{\varphi}_j(x)$ and $\varphi_j(x)$ decrease, as well as the mode-scaling factor value (Figure 3). Here, the strain mode shapes of the SFT are from one of the models investigated in numerical validation section.

2.2 Strain-displacement transformation

Figure 1 depicts an example of an SFT with strain gauges installed at N midspan locations along the tunnel ($x = x_{m,i}, i = 1, \cdots, N$). At the cross section of each location, three strain gauges (S1–S3) are attached at three different points along the vertical (z) and horizontal (y) directions. The measurements from strain gauges S1, S2, and S3 are denoted as ε_k^1, ε_k^2, and ε_k^3. Here, subscript k denotes the kth time step. Based on a mode superposition algorithm [16], the strain measurements ε_k^1 and ε_k^2 can be transformed into vertical displacement ($u_k^z(x)$) as follows:

$$u_k^z(x) = \frac{1}{h} \begin{bmatrix} \psi_1^z(x) \\ \vdots \\ \psi_N^z(x) \end{bmatrix}^T \begin{bmatrix} \varphi_1^z(x_{m,1}) & \cdots & \varphi_N^z(x_{m,1}) \\ \vdots & \ddots & \vdots \\ \varphi_1^z(x_{m,N}) & \cdots & \varphi_N^z(x_{m,N}) \end{bmatrix}^{-1} \begin{bmatrix} \Delta\varepsilon_k^{1,2}(x_{m,1}) \\ \vdots \\ \Delta\varepsilon_k^{1,2}(x_{m,N}) \end{bmatrix} \tag{2}$$

$$\Delta\varepsilon_k^{1,2}(x_{m,i}) = \varepsilon_k^1(x_{m,i}) - \varepsilon_k^2(x_{m,i}); i = 1, \cdots, N \tag{3}$$

where h denotes the vertical distance between strain gauges S1 and S2. Using the simplified strain and displacement mode shapes, Equation (2) becomes

$$u_k^z(x) = \frac{1}{h}\begin{bmatrix}\bar{\psi}_1(x)\\\vdots\\\bar{\psi}_N(x)\end{bmatrix}^T\begin{bmatrix}\frac{1}{\alpha_1^z} & & \\ & \ddots & \\ & & \frac{1}{\alpha_N^z}\end{bmatrix}\begin{bmatrix}\bar{\varphi}_i(x_{m,1}) & \cdots & \bar{\varphi}_N(x_{m,1})\\\vdots & \ddots & \vdots\\\bar{\varphi}_i(x_{m,N}) & \cdots & \bar{\varphi}_N(x_{m,N})\end{bmatrix}^{-1}\begin{bmatrix}\Delta\varepsilon_k^{1,2}(x_{m,1})\\\vdots\\\Delta\varepsilon_k^{1,2}(x_{m,N})\end{bmatrix}$$

(4)

Equation (4) involves N mode-scaling factors, and their estimation is discussed in section 3.1. Similarly, the horizontal displacement (u_k^y) can be estimated from the strain measurements ε_k^1 and ε_k^3.

3. Development of displacement and tension force estimation technique for SFTs

This section proposes a simultaneous displacement and cable tension estimation technique for SFTs, using strain and acceleration measurements. As shown in Figure 2, the proposed technique consists of two steps: (1) automated mode-scaling factor estimation (Section 3.1), and (2) continuous displacement and mooring cable tension force estimation (Section 3.2). Note that the mode-scaling factor and displacement estimation steps are explained only for vertical displacement, but these steps can be easily extended to estimate the horizontal displacement as well.

3.1. Automated mode-scaling factor estimation

An automated algorithm is proposed in this section to estimate the values of the unknown mode-scaling factors in Equation 4, which are necessary for the strain-displacement transformation. Note that out of N unknown mode-scaling factors, only the first P ($<N$) scaling factors are estimated, and the remaining high-order scaling factor values are set to 1. This approximation can be justified on the basis of (1) the difference between the simplified and true mode shapes, and (2) the contribution of the higher modes to the structural displacement, where both decrease as the mode order increases (Figure 3). It should be noted that because at least P equations are needed for the estimation of P mode-scaling factors, Equation (4) is extended to include displacement estimation at P locations ($x_{d,i}, 1 \le i \le P$):

$$\begin{bmatrix}u_k^z(x_{d,1})\\\vdots\\u_k^z(x_{d,P})\end{bmatrix} = \frac{\bar{\boldsymbol{\psi}}_{Full}}{h}\begin{bmatrix}\frac{1}{\alpha_1^z} & & & & \\ & \ddots & & & \\ & & \frac{1}{\alpha_P^z} & & \\ & & & 1 & \\ & & & & \ddots & \ddots \\ & & & & & 1\end{bmatrix}\begin{bmatrix}\bar{\varphi}_1(x_{m,1}) & \cdots & \bar{\varphi}_N(x_{m,1})\\\vdots & \ddots & \vdots\\\bar{\varphi}_1(x_{m,N}) & \cdots & \bar{\varphi}_N(x_{m,N})\end{bmatrix}^{-1}\begin{bmatrix}\Delta\varepsilon_k^{1,2}(x_{m,1})\\\vdots\\\Delta\varepsilon_k^{1,2}(x_{m,N})\end{bmatrix}$$

(5)

$$\bar{\boldsymbol{\psi}}_{Full} = (\bar{\boldsymbol{\psi}}_{Low}|\bar{\boldsymbol{\psi}}_{High}) = \begin{bmatrix}\begin{pmatrix}\bar{\psi}_1(x_{d,1}) & \cdots & \bar{\psi}_P(x_{d,1})\\\vdots & \ddots & \vdots\\\bar{\psi}_1(x_{d,P}) & \cdots & \bar{\psi}_P(x_{d,P})\end{pmatrix}\Bigg|\begin{pmatrix}\bar{\psi}_{P+1}(x_{d,1}) & \cdots & \bar{\psi}_N(x_{d,1})\\\vdots & \ddots & \vdots\\\bar{\psi}_{P+1}(x_{d,P}) & \cdots & \bar{\psi}_N(x_{d,P})\end{pmatrix}\end{bmatrix}$$

(6)

3.1.1 Transformation equation decoupling

First, Equation (5) is decoupled into P independent equations before estimating the values of the mode-scaling factors. The strain-based modal responses ($\bar{q}_{j,k}^s$, $1 \le j \le P$) are defined as follows.

$$
\begin{bmatrix} \bar{q}_{1,k}^s \\ \vdots \\ \bar{q}_{N,k}^s \end{bmatrix} = \frac{1}{h} \begin{bmatrix} \bar{\varphi}_1(x_{m,1}) & \cdots & \bar{\varphi}_N(x_{m,1}) \\ \vdots & \ddots & \vdots \\ \bar{\varphi}_1(x_{m,N}) & \cdots & \bar{\varphi}_N(x_{m,N}) \end{bmatrix}^{-1} \begin{bmatrix} \Delta\varepsilon_k^{1,2}(x_{m,1}) \\ \vdots \\ \Delta\varepsilon_k^{1,2}(x_{m,N}) \end{bmatrix} \tag{7}
$$

The following equation is obtained by introducing Equation (7) into Equation (5):

$$
\boldsymbol{u}_k^z = \begin{bmatrix} u_k^z(x_{d,1}) \\ \vdots \\ u_k^z(x_{d,P}) \end{bmatrix} = \bar{\boldsymbol{\psi}}_{Low} \begin{bmatrix} \dfrac{1}{\alpha_1^z} & & \\ & \ddots & \\ & & \dfrac{1}{\alpha_P^z} \end{bmatrix} \begin{bmatrix} \bar{q}_{1,k}^s \\ \vdots \\ \bar{q}_{P,k}^s \end{bmatrix} + \bar{\boldsymbol{\psi}}_{High} \begin{bmatrix} \bar{q}_{P+1,k}^s \\ \vdots \\ \bar{q}_{N,k}^s \end{bmatrix} \tag{8}
$$

Equation (8) can be further rewritten as,

$$
\begin{bmatrix} q_{1,k}^u \\ \vdots \\ q_{P,k}^u \end{bmatrix} = \begin{bmatrix} \dfrac{1}{\alpha_1^z} & & \\ & \ddots & \\ & & \dfrac{1}{\alpha_P^z} \end{bmatrix} \begin{bmatrix} \bar{q}_{1,k}^s \\ \vdots \\ \bar{q}_{P,k}^s \end{bmatrix} = (\bar{\boldsymbol{\psi}}_{Low})^{-1} \left\{ \boldsymbol{u}_k^z - \bar{\boldsymbol{\psi}}_{High} \begin{bmatrix} \bar{q}_{P+1,k}^s \\ \vdots \\ \bar{q}_{N,k}^s \end{bmatrix} \right\} \tag{9}
$$

where $q_{j,k}^u$ denotes the jth modal response decomposed from $\boldsymbol{u}_k^z$ after removing the high-order ($>P$) modal responses. Finally, P independent equations are obtained, and each of them includes only one mode-scaling factor.

$$
q_{j,k}^u = \bar{q}_{j,k}^s / \alpha_j^z; \; j = 1, \cdots, P \tag{10}
$$

3.1.2 Mode-scaling factor estimation

Assuming that accelerometers are installed at P locations and strain gauges are installed at N locations, a flowchart of the proposed mode-scaling factor estimation algorithm is presented in Figure 4. Note that the strain gauges must be installed at the mid-span locations of each tunnel segment, whereas the accelerometers can be installed at arbitrary locations along the tunnel.

First, $\Delta\varepsilon_k^{1,2}(x_{m,i})$ for $i = 1, \cdots, N$, are computed from strain measurements using Equation (3), and high-pass filtered. Subsequently, the high-pass filtered $\Delta\varepsilon_k^{1,2}(x_{m,i})$ are decomposed into strain-based modal responses ($\bar{q}_{i,k}^s$) using Equation (7). The strain-based modal responses are divided into two parts: (1) high-order ($j > P$) and (2) low-order ($j \le P$).

Second, high-frequency displacements are estimated at P locations by double integrating and high-pass filtering acceleration measurements. Then, acceleration-based low-order modal responses

$(q_{j,k}^u, 1 \le j \le P)$ are estimated from the acceleration-based high-frequency displacements and high-order ($\bar{q}_{j,k}^s, j > P$) strain-based modal responses using Equation (9).

Assuming that both the acceleration and strain are measured for a short time (less than 1 min), $q_{j,k}^u$ and $\bar{q}_{j,k}^s$ are obtained at multiple time steps. Therefore, α_j^z can be estimated as the slope of the $\bar{q}_{j,k}^s$ vs. $q_{j,k}^u$ plot using least-squares regression. The purpose of high-pass filtering is to remove large low-frequency drifts in the acceleration-based displacements. The cut-off frequency of the filter should, therefore, be sufficiently high to remove drifts and should be lower than the first resonance frequency of the SFT. Note that an identical high-pass filter should be applied to both strain and acceleration measurements.
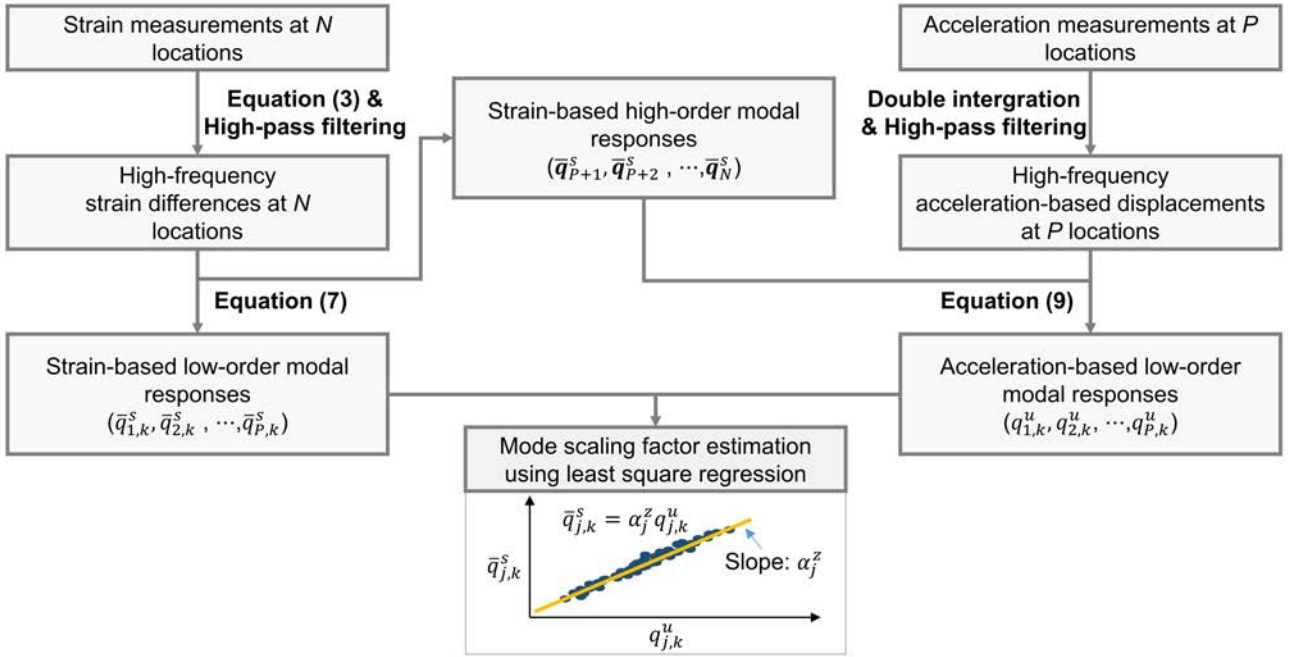

Figure 4. Flowchart of proposed mode-scaling factor estimation algorithm.

3.2. Continuous displacement and mooring cable tension force estimation

After estimating the mode-scaling factors using the initial acceleration and strain measurements, the displacement and mooring cable tension force can be continuously monitored.

3.2.1 FIR filter-based displacement estimation

Displacement estimated from acceleration measurement using the double integration has a low-frequency drift caused by unknown initial conditions and measurement noises. A high-pass filter can be used to remove the low-frequency drift [11], but it also removes the low-frequency structural displacement. Displacement estimated from strain measurement usually have low accuracy owing to relatively large noise levels in strain measurement [12,13]. An FIR filter was adopted in this study to estimate the SFT displacement by fusing strain and acceleration measurements, and the final displacement is estimated as a combination of low-frequency displacement from strain measurements

and high-frequency displacement from acceleration measurements, which provides better accuracy than strain-based displacement. Figure 5 presents a flowchart of the proposed FIR filter-based technique, assuming that strain gauges are installed at N mid-span locations and an accelerometer is installed at the target location where displacement needs to be estimated.

First, multiple strain measurements are transformed into displacement at the target location using Equation (4) and the estimated mode-scaling factors. The strain-based displacement is then filtered using a low-pass filter (C_L) to obtain low-frequency displacement, while the high-frequency displacement is obtained from double integration and the high-pass filtered acceleration measurements, where double integration and high-pass filtering are simultaneously performed by C_H. The cutoff frequencies of the low-pass and high-pass filters are set to the first resonance frequency of the SFT. More details on C_L and C_H can be found in the Appendix and Park *et.al.* [16]. The final displacement is obtained by combining the high-frequency displacement obtained from the acceleration measurement and the low-frequency displacement obtained from the strain measurements.
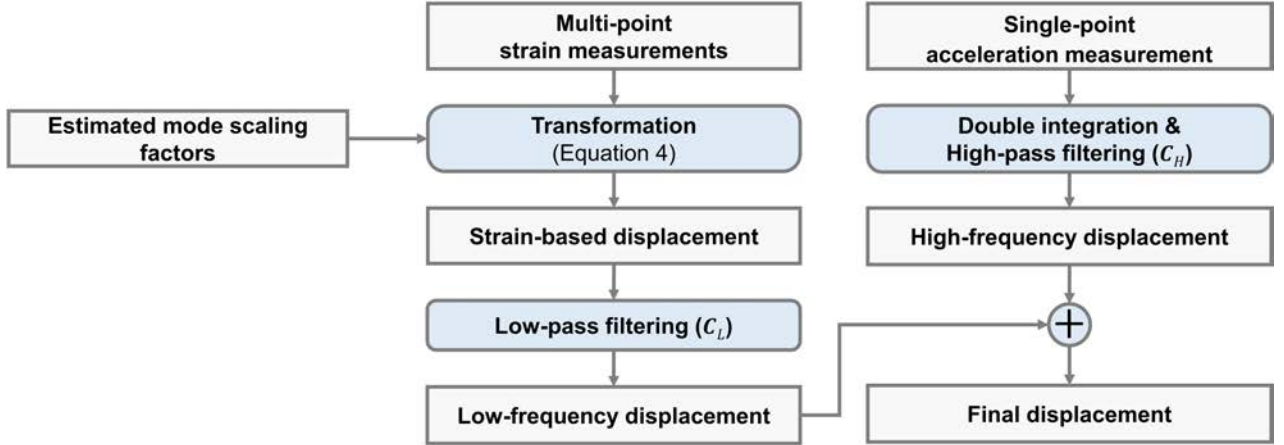

Figure 5. Flowchart of FIR filter-based continuous displacement estimation by combining strain and acceleration measurements.

3.2.2 Mooring cable tension force estimation

The tension force of the mooring cable is estimated from both the horizontal and vertical displacements at the connection point between the tunnel and mooring cable. For the SFT shown in Figure 6, the following equation can be derived from the geometric relationship between the initial ($t = 0$) and current state ($t = k\Delta t$) of the SFT:

$$\sqrt{\{y_0 + u_k^y - R\}^2 + \{z_0 + u_k^z\}^2} = L_k^l; \quad \sqrt{\{y_0 + u_k^y + R - D_y/2\}^2 + \{z_0 + u_k^z\}^2} = L_k^r \qquad (11)$$

where R denotes the outer radius of the tunnel, and D_y denotes the distance between two anchoring points along the y-direction. $\{y_0, z_0\}$ denotes the initial position of the center of the tunnel cross-section. L_k^l and L_k^r denote the lengths of the left and right cables at the kth time step, respectively.

L_k^l and L_k^r are related to the initial lengths (L_0^l and L_0^r), axial stiffness (K), and tension forces (T_k^L and T_k^r) of the two cables, as follows:

$$L_k^l = \left\{1 + \frac{T_k^l}{K}\right\} L_0^l; \ L_k^r = \left\{1 + \frac{T_k^r}{K}\right\} L_0^r \tag{12}$$

By combining Equations (11) and (12), the tension forces can be estimated as follows:

$$T_k^L = \left(\sqrt{\{y_0 + u_k^y - R\}^2 + \{z_0 + u_k^z\}^2} - L_0^l \right) K / L_0^l;$$

$$T_k^r = \left(\sqrt{\{y_0 + u_k^y + R - D_y/2\}^2 + \{z_0 + u_k^z\}^2} - L_0^r \right) K / L_0^r \tag{13}$$

Note that the mooring cables are assumed to be straight without any sag and are always in tension because of the large initial tension.
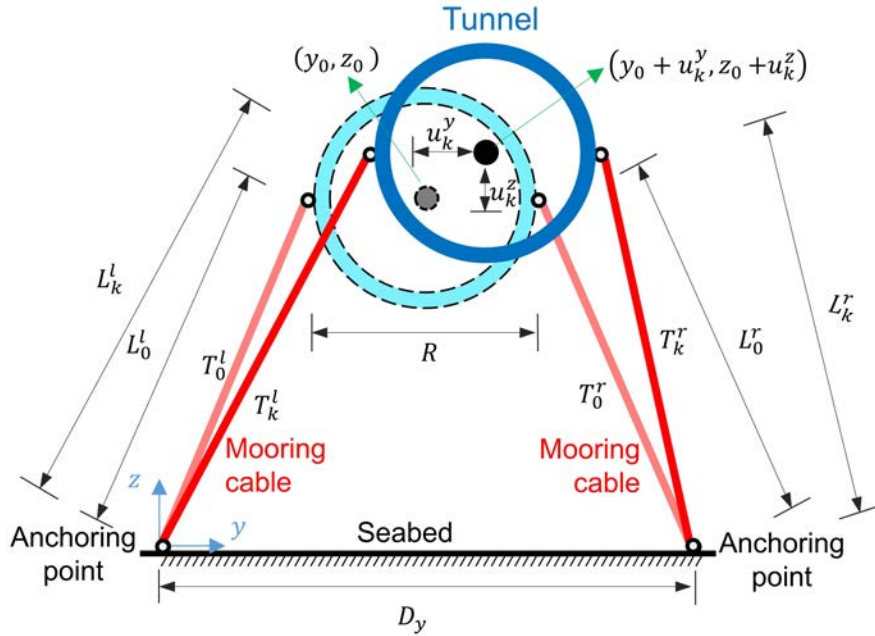

Figure 6. Relationship between the tunnel displacement and the anchoring positions of two mooring cables

4. Numerical Validation

4.1 Model description

Figure 7(a) shows the model for an SFT, which consists of an 800 m long tunnel and 54 m long mooring cables spaced every 50 m along the longitudinal direction of the tunnel. The tunnel was modeled in ABAQUS with the B31 beam element, and the mooring cables were modeled with the T3D2 truss element, similar to existing studies [31,32]. The simply supported boundary condition, which has been widely used in previous studies [4,31,32], was adopted for the tunnel. The different boundary conditions are investigated in Section 4.4.5. Strain gauges were installed at seven mid-span

locations (*i.e.,* 5, 9, 13, 15, 19, 23, and 27), and accelerometers were installed at locations 1–31, where the displacement needed to be estimated, as shown in Figure 7(a). Note that these thirty-one locations are either the connection points between the cable and tunnel or the mid-span locations. Additional parameters regarding the tunnel and mooring cables are shown in Figure 7(b), and the values reported in previous studies [31,33] are used here. The gravity and buoyancy of the tunnel were 1.065×10^6 kN and 2.199×10^6 kN, respectively. The remaining buoyancy of 1.134×10^6 kN was balanced by 30 mooring cables, resulting in 3.78×10^4 kN initial tension force for each mooring cable.
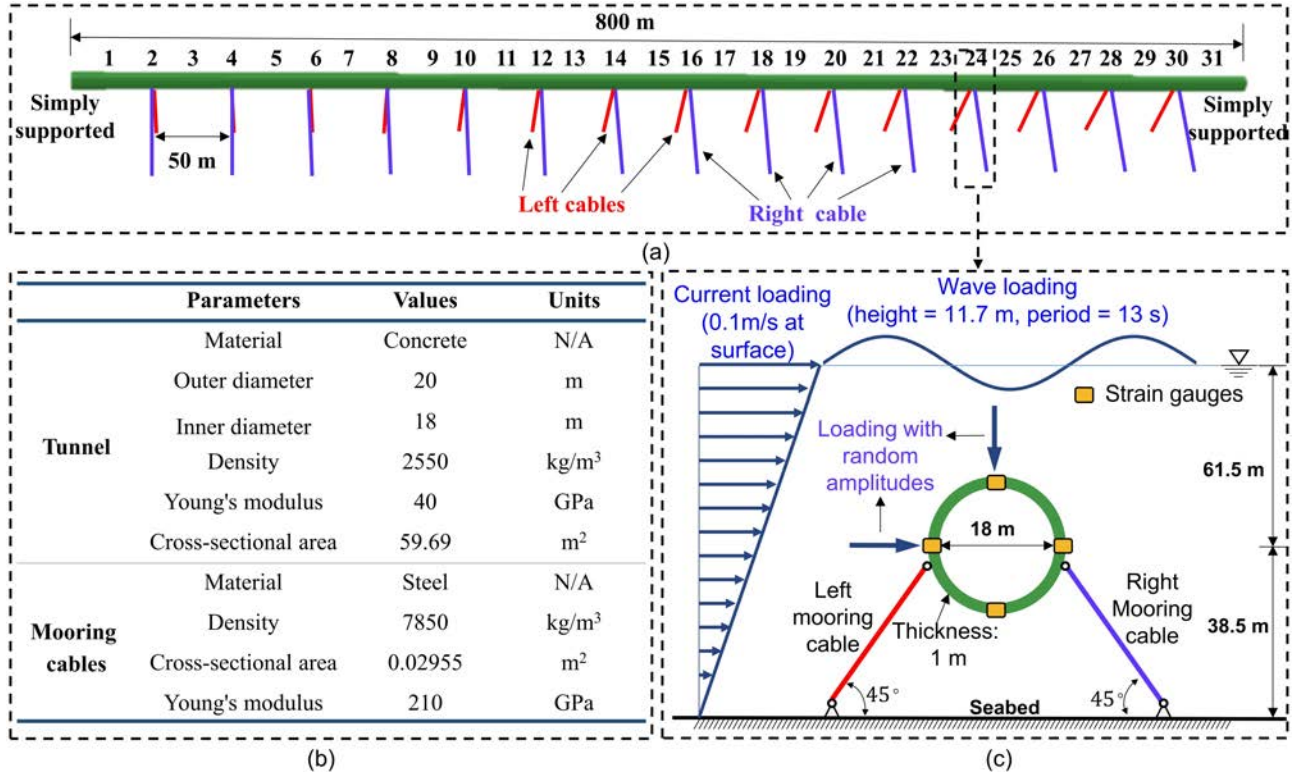

Figure 7. Numerical simulation of an SFT model in ABAQUS: (a) overview of the model and sensor setup, (b) design parameters of the model, and (c) cross-sectional view of the model and hydrodynamic environment considered for the model.

As shown in Figure 7(c), strain gauges were installed at four points on each cross-section at locations 5, 9, 13, 15, 19, 23 and 27, for horizontal and vertical displacement estimations. Note that for the B31 beam element, only the strain responses at these four points are available in ABAQUS. The tunnel had a tubular cross-section with an inner diameter of 18 m and a thickness of 1 m. One end of the mooring cable, inclined at 45°, was pin-connected to the tunnel and the other end to the seabed. The distances from the tunnel to the seabed and the water surface were set to 38.5 m and 61.5 m, respectively, similar to the previous studies [33–35]. The SFT model was simultaneously subjected to (1) wave and current loadings, and (2) uniformly distributed loading with random amplitudes in both the horizontal and vertical directions, as shown in Figure 7(c). The hydrodynamic environment was simulated using ABAQUS/Aqua, which has been commonly used in previous studies [36–38]. However, the real hydrodynamic environment may be more complex [39], and more research is needed to consider this.

Then, the corresponding acceleration, strain, displacement responses, and cable tension forces were simulated for 100 s at a sampling rate of 100 Hz. The simulated displacement and cable tension force were used as reference values to evaluate the estimation performance of the proposed technique. The current velocity decreased linearly from 0.1 m/s at the water surface to 0 at the seabed. The wave height and period were 11.7 m and 13 s, respectively. The hydrodynamic environment was simulated using ABAQUS/Aqua.

4.2 Mode-scaling factor estimation results

Strain gauges were installed at seven locations, and seven modes were extracted. Mode-scaling factors were estimated from the first three modes ($P = 3$) using the 30 s acceleration responses recorded at three locations (*i.e.,* 5, 15, and 27) and strain responses at all seven locations. Because the first resonance frequency of the SFT was 0.35 Hz, the cut-off frequency of the high-pass filter required for the mode-scaling factor estimation was set to 0.30 Hz. As shown in Figure 8(a), three different modal responses at 0.35 Hz, 0.49 Hz, and 0.96 Hz were decomposed from strain and acceleration measurements using Equations (7) and (9), respectively.
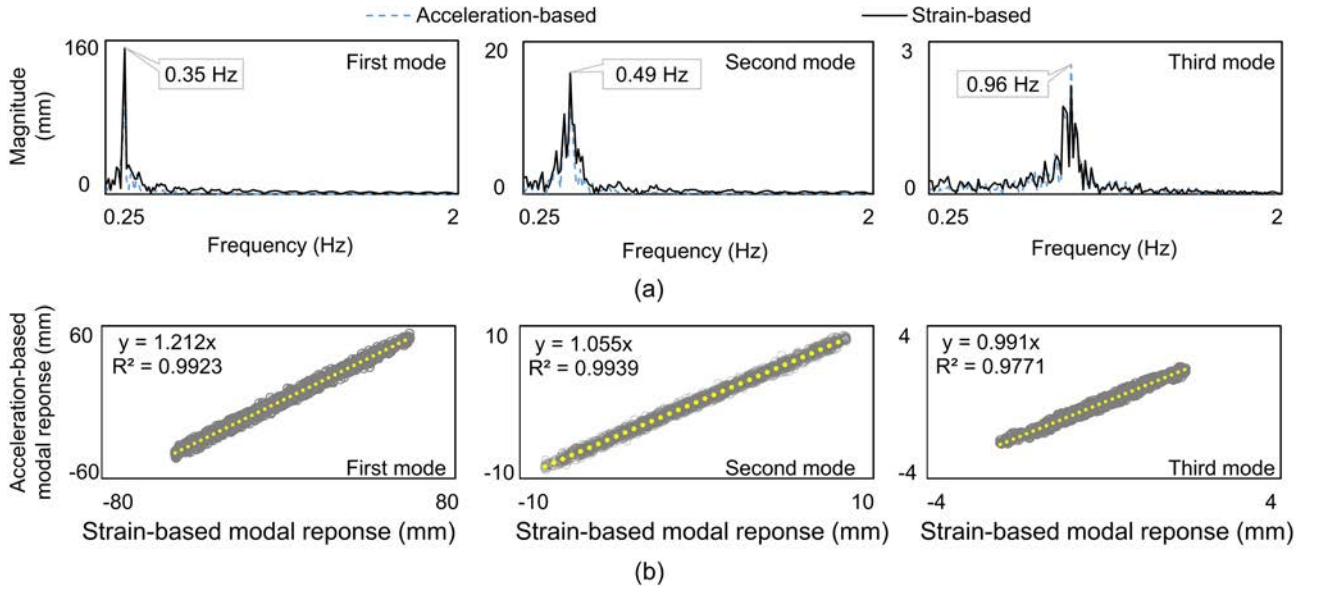

Figure 8. (a) Decomposed modal responses using Equations (7) and (9) and (b) Estimated mode-scaling factors based on Equation (10) using the first 30 s acceleration responses at three locations (*i.e.,* 5,15, and 27) and strain responses at seven locations (*i.e.,* 5, 9, 13, 15, 19, 23 and 27)

Here, only the first three modes were used for the displacement estimation because the contribution of the lower modes is more significant than that of the higher modes. That is, as the mode order increases, the magnitude of the modal responses decreases significantly. For example, the response amplitude of the third-order mode was only 1.4% of the first-order mode response. The corresponding scale-factor estimation results are shown in Figure 8(b). Apparent linear relationships were observed between the acceleration- and strain-based modal responses, with R^2 values greater than 0.97. Note

that all results in this section were obtained in the vertical direction, and similar results obtained in the horizontal direction were omitted here owing to space limitations.
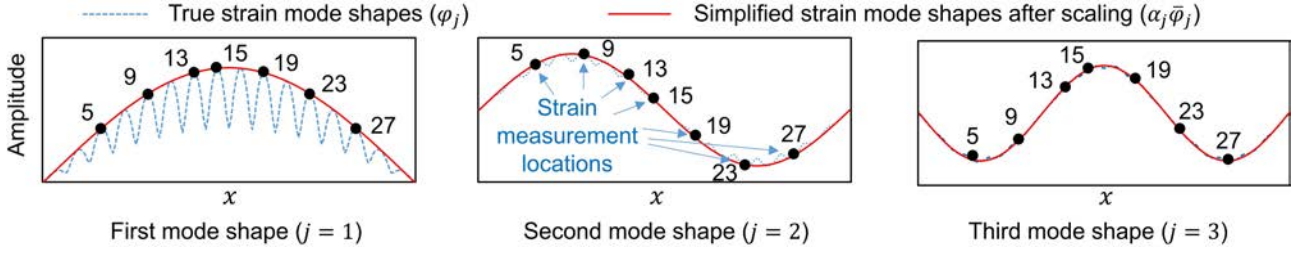

Figure 9. Comparison of true strain mode shapes and simplified mode shapes of the SFT model after amplitude scaling.

Figure 9 shows a comparison of the first three true strain mode shapes of the SFT model and the corresponding simplified strain mode shapes. As mentioned in Section 2.1, the discrepancy decreased from the first mode shape to the third mode shape, and the difference was negligible for the third mode. Even for the first mode shape, good agreement was observed at mid-span locations (*i.e.,* locations 5, 9, 13, 15, 19, 23, and 27) after scaling of the simplified first mode. Therefore, the use of simplified strain mode shapes is acceptable if the strain responses at mid-span locations are used. For the SFT model used in this simulation, the stiffness ratio defined in Equation (1) was 0.0122, which is close to the values used in Jin et al. al. [36], and Kim et. al.[4] (0.0125 and 0.013). The effect of the stiffness ratio on the displacement estimation accuracy is discussed in Section 4.4.4.

4.3 Displacement and tension force estimation results

4.3.1 Displacements

The cutoff frequency of the FIR filters was set to the first resonance frequency of the SFT, *i.e.,* 0.35 Hz. The displacement at location 1 was estimated using the acceleration response at this location and the strain responses at locations 5, 9, 13, 15, 19, 23, and 27. This procedure was repeated for all thirty-one locations where accelerometers were placed to estimate the displacements at all locations. Figure 10 shows the displacements estimated at the middle of the tunnel (location 15) using the proposed and existing techniques [16]. The existing technique first transforms strain measurements to displacement using the assumed mode shapes and then simultaneously estimates the final displacement and a scaling factor, used to compensate for the discrepancy between the true and assumed mode shapes from the transformed displacement and acceleration measurement by integrating the FIR filter with a recursive least square (RLS) algorithm. The displacements estimated using both techniques agreed closely with the reference displacements. Note that the existing technique computes a single scaling factor for all modes, but the scaling factor value varies with respect to the displacement estimation locations. In contrast, the proposed technique computes different scaling factors for each mode; however, each scaling factor value was constant at all locations. The estimated displacements from 15 to 18 s were

magnified on the right-hand side of Figure 10 to clearly show the differences between the estimated and reference displacements.
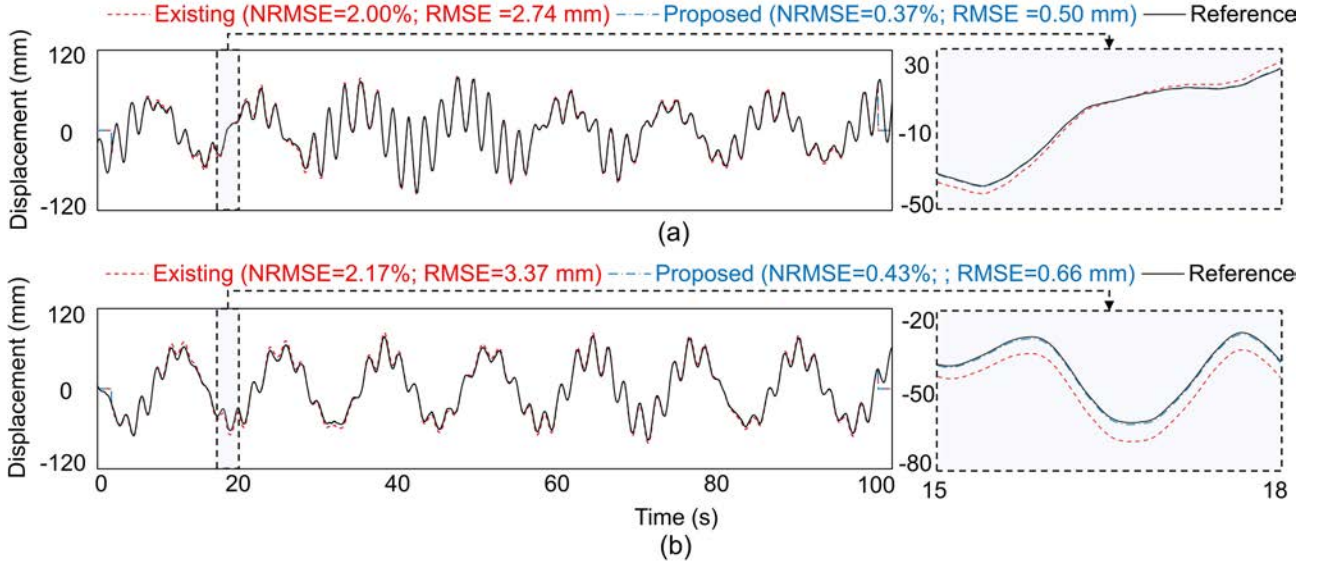

Figure 10. Comparison of (a) vertical and (b) horizontal displacements estimated from the proposed and existing techniques [16] at location 15 of the numerical SFT model.

The displacement estimation performance was quantitatively evaluated using the root mean square error (RMSE) and normalized RMSE (NRMSE) as follows:

$$\text{RMSE } (mm) = \sqrt{\frac{\sum_{k=1}^{Q}\{(u_k^r - u_k)^2\}}{Q}}; \ \text{NRMSE } (\%) = 100 \frac{\text{RMSE}}{\max(u_k^r) - \min(u_k^r)} \qquad (14)$$

where u_k^r and u_k denote the reference and estimated displacements at the kth time step, respectively, and Q is the number of data points. The proposed technique estimated displacements with NRMSE and RMSE values of less than 0.5% and 0.7 mm, respectively. Note that the NRMSE and RMSE values of the proposed technique were only one-fifth those of the existing technique.

Figure 11 summarizes the NRMSE and RMSE values of the estimated horizontal and vertical displacements at all thirty-one locations. The proposed technique had smaller NRMSE and RMSE values than the existing technique at most locations. The NRMSE and RMSE values achieved by the proposed method were below 1% and 1 mm, respectively, in both horizontal and vertical directions. In addition, the displacement estimation accuracy of the proposed technique was less sensitive to the displacement estimation location than that of the existing technique, and a similar level of performance was achieved at all locations. Note that the proposed technique estimated only three location-independent mode-scaling factors, whereas the existing technique required thirty-one location-dependent scaling factors to estimate the displacement at thirty-one locations.
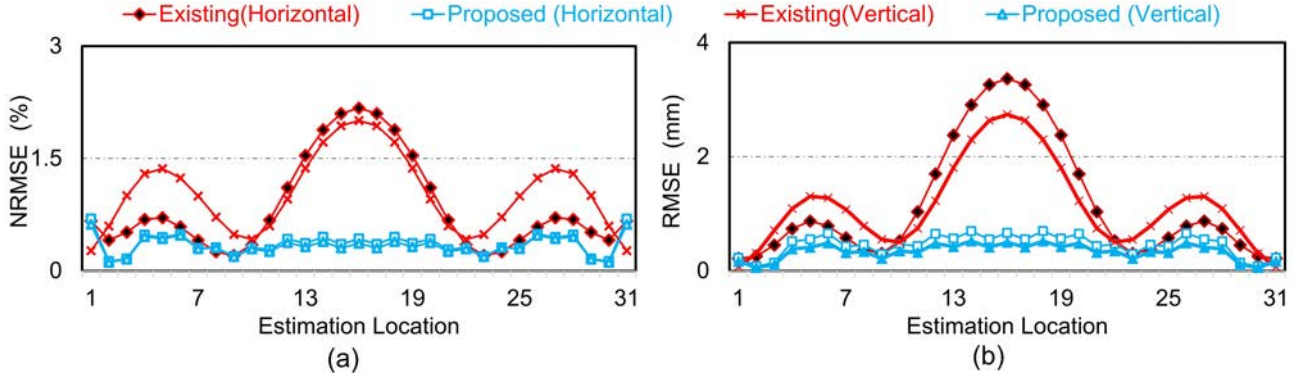
Figure 11. Comparison of (a) NRMSE and (b) RMSE of displacements estimated by the proposed and existing techniques at different locations of the numerical SFT model.
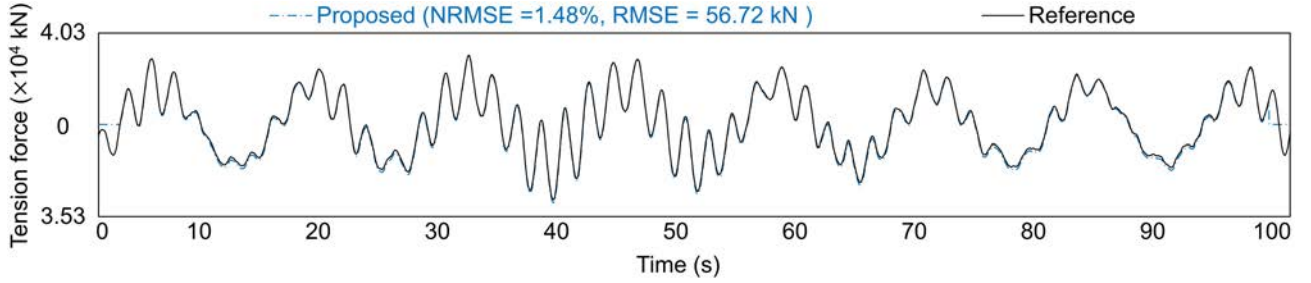
4.3.2 Tension forces

Figure 12. Tension force estimated using the proposed technique for the left mooring cable at location 16 of the numerical SFT model.

The displacement estimated at the connection point between the tunnel and mooring cable was used to estimate the tension force of the corresponding mooring cable. Figure 12 shows the tension force estimated at the left mooring cable for location 16. Good agreement was observed between the estimated and reference tension forces. Figure 13 summarizes the NRMSE values of the tension forces estimated for all mooring cables. The proposed technique showed less than 2% NRMSE and 60 kN RMSE for all mooring cables.
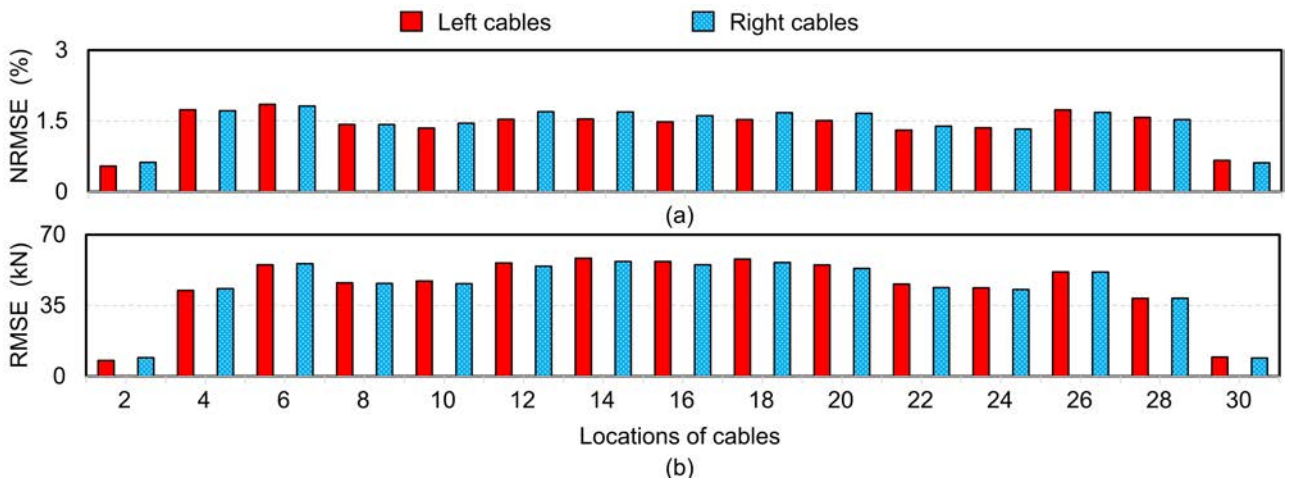

Figure 13. Comparison of (a) NRMSE and (b) RMSE values of tension forces estimated at all mooring cables of the numerical SFT model.

4.4 Parametric study on the displacement estimation accuracy
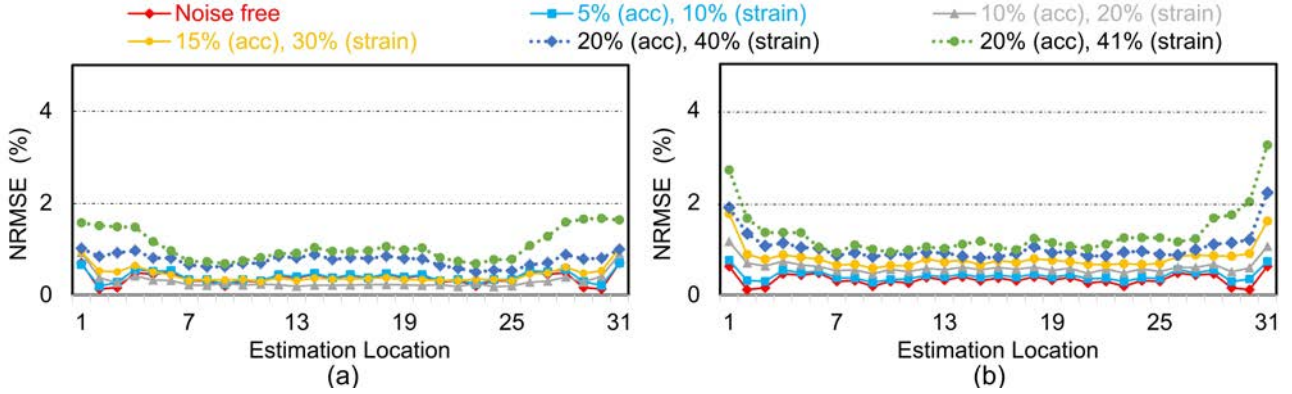
4.4.1 Measurement noises

Figure 14. Accuracy of (a) vertical and (b) horizontal displacements estimated along the longitudinal direction of the tunnel under varying strain and acceleration measurement noise levels

Different levels of Gaussian white noise were added to the acceleration and strain responses to examine the effect of measurement noise on the displacement measurement accuracy. Because accelerometers typically have higher signal-to-noise ratios (SNRs) than strain gauges, the SNR of the acceleration responses was set to twice that of the strain responses. Figure 14 summarizes the displacement estimation performance under different measurement noise levels. Although the displacement estimation error increased with the measurement noise level, it was still less than 2% at most locations. Note that the NRMSE values were relatively large near the two fixed ends because of the relatively small displacements at these locations, particularly in the horizontal direction. However, the absolute displacement errors at these locations were very small, less than 1.5 mm.

4.4.2 Values of P and N

First, the displacements were estimated by varying the N value from one to nine. The corresponding RMSEs of the estimated displacements are shown in Figure 15. Significant RMSE reductions were observed when N increased from one to seven. However, further increases beyond seven did not improve the NRMSE value much. The P value was set to one when N equaled one, and to three in other cases.
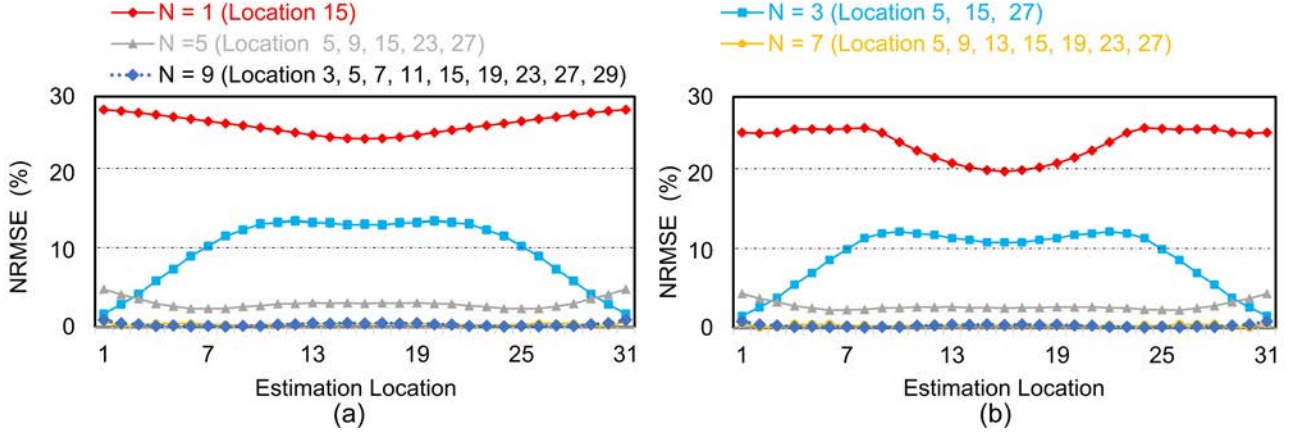
Figure 15. Accuracy of (a) vertical and (b) horizontal displacements estimated along the longitudinal direction of the tunnel with varying *N* values.
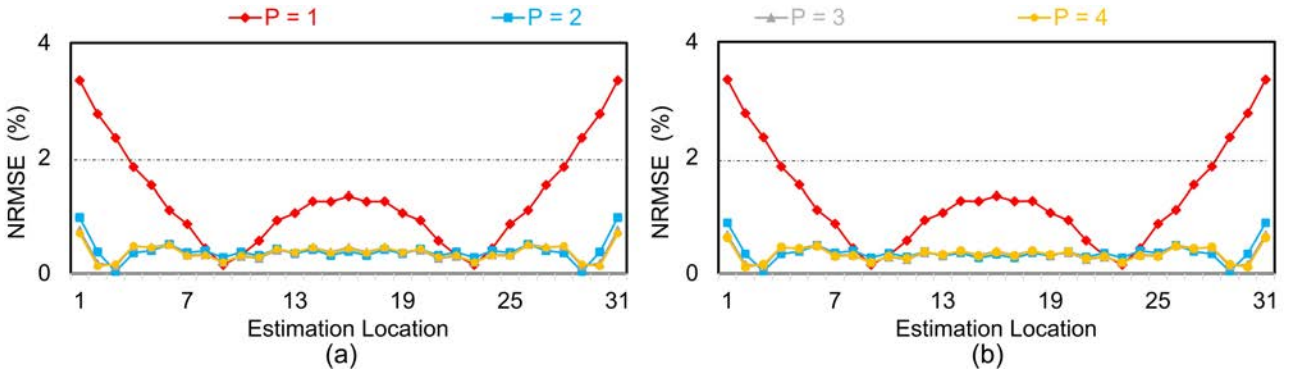

Figure 16. Accuracy of (a) vertical and (b) horizontal displacements estimated along the longitudinal direction of the tunnel with varying *P* values.

Next, the *N* value was fixed at seven, and the displacements were estimated by varying the *P* value. The corresponding NRMSE values of the estimated displacements are shown in Figure 16. Increasing the *P* value from one to two resulted in a significant decrease in the NRMSE value. However, further increase of the *P* value did not reduce the NRMSE value much. This observation is consistent with Figure 8(a). As the mode order increases, the magnitude of the modal responses decreases significantly. Therefore, setting the values of the high-order scaling factors to one did not cause a significant difference.

4.4.3 Wave period

The wave period was changed from 13 s to 3 s, 7 s, 25 s, and 40 s, and the corresponding displacements were estimated using the proposed technique. It should be noted that the SFT model at low frequencies is mainly excited by wave loading. The SFT model had low-frequency vibration at different frequencies when the wave period was changed. Figure 17 summarizes the displacement estimation accuracies for different wave periods. Although slight differences were observed, the proposed technique estimated displacement accurately with less than 1% NRMSE in all cases.
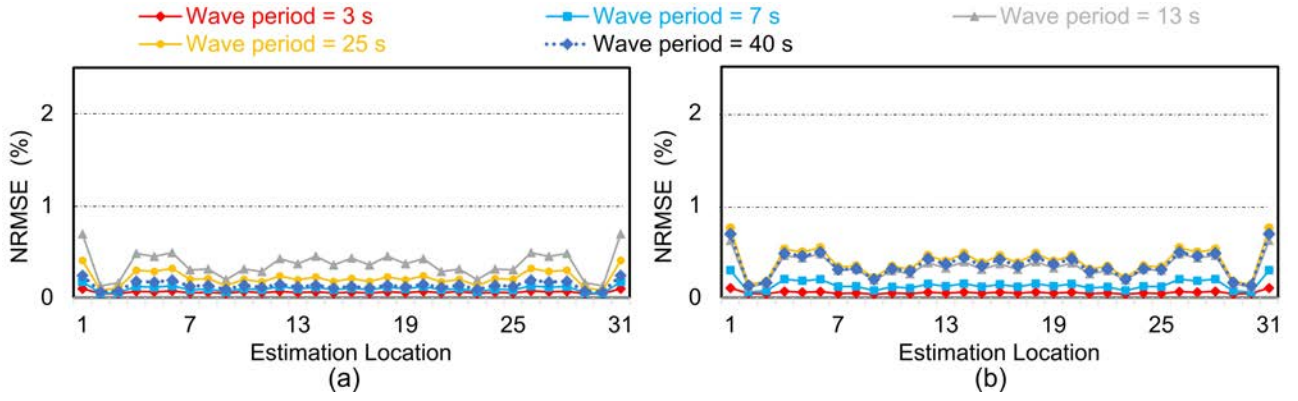
Figure 17. Accuracy of (a) vertical and (b) horizontal displacements estimated along the longitudinal direction of the tunnel under varying wave period.
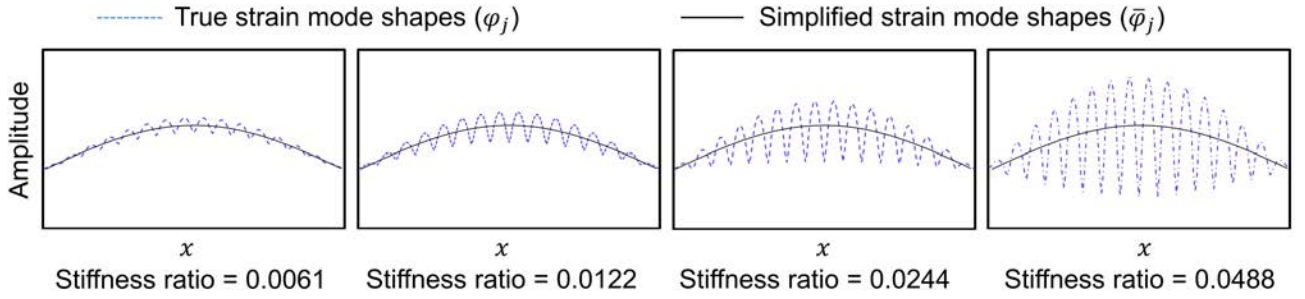
4.4.4 Stiffness ratio

Figure 18. Comparison of the true and simplified first mode shapes of the SFT models under varying stiffness ratios

Figure 19. Accuracy of (a) vertical and (b) horizontal displacements estimated along the longitudinal direction of the tunnel under varying stiffness ratios

Three additional SFT models with different stiffness ratios were simulated by changing the stiffness of the mooring cables. Similar effects can be obtained by changing the distance between two adjacent mooring cables or the bending stiffness of the tunnel. Note that the stiffness ratios of all models still satisfy Equation (1). The displacements were estimated for the four SFT models following the procedures described in Section 4.1, except for the stiffness ratios. Figure 18 compares the true and simplified first-mode shapes of the four SFT models. Apparently, the discrepancy increases as the

stiffness ratio increases, resulting in larger mode-scaling factors. For all models, the proposed technique estimated displacement with less than 2% NRMSE as shown in Figure 19.

4.4.5 Boundary condition

By changing the boundary conditions of the tunnel from hinged at both ends to fixed at both ends, and fixed at one end and hinged at the other, two additional SFT models were simulated. Note that the real-world construction of an SFT has not yet been realized, and most existing studies have adopted either simply supported [4,31,32] or fixed-fixed [3,33,35,40] boundary conditions. Figure 20 summarizes the accuracy of displacement estimation. Because the simplified mode shapes were obtained with simply supported boundary conditions, large discrepancies between the simplified and true mode shapes appeared at locations near the two ends, *i.e.,* locations 1–3 and 29–31 for the SFT model with fixed boundaries at both ends. Therefore, large NRMSE and RMSE values were observed at these six locations (1–3 and 29–31). For the remaining 25 locations, NRMSE values obtained using the proposed technique were below 0.8%. When the SFT model was fixed at one end and hinged at the other, extremely large errors were observed near the fixed end, *i.e.,* at locations 1–3. Except for these three locations, displacements were still reliably estimated at the remaining 28 locations, with RMSE values less than 2.4 %. Much larger errors were observed from the SFT model fixed at one end and hinged at the other owing to its nonsymmetric mode shapes.
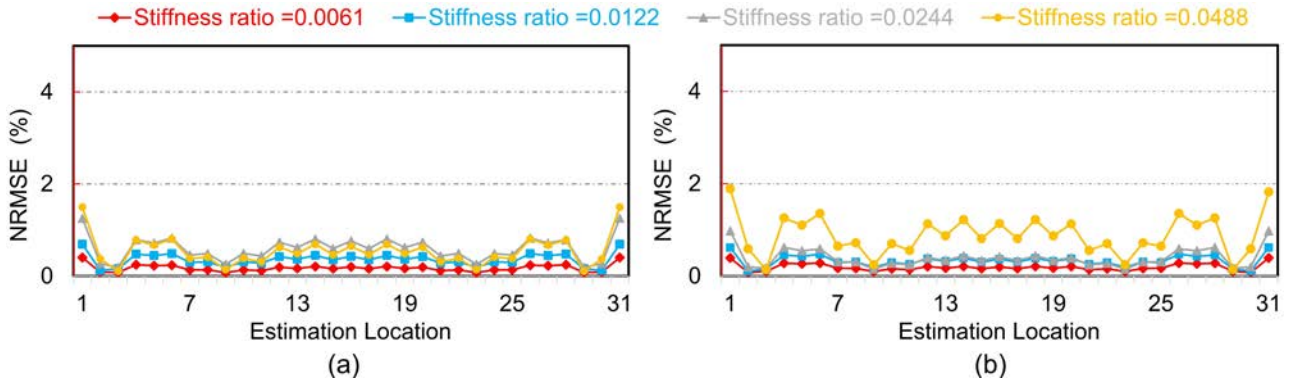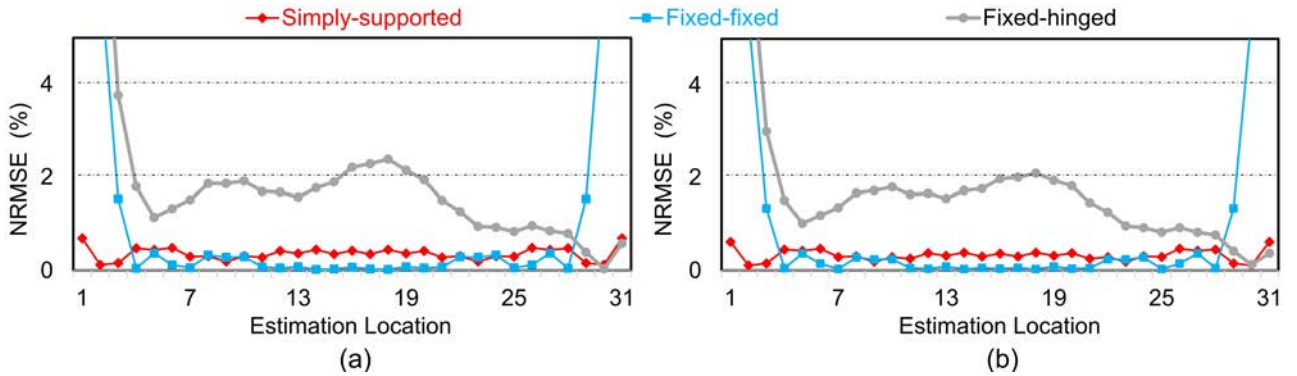

Figure 20. Accuracy of (a) vertical and (b) horizontal displacements estimated along the longitudinal direction of the tunnel under varying boundary conditions.

5. Experimental Validation

5.1 Experimental setup

To further validate the performance of the proposed technique, a laboratory test was conducted on an 8 m long SFT mock-up structure. The tunnel consisted of eight bolt-connected aluminum tubes. Note that the Young's modulus and density of the tube were 70 GPa and 2710 kg/m^3, respectively. Each tube was 1 m long and had a uniform circular cross section with an inner diameter of 13 cm and a thickness of 0.5 cm. The tunnel was submerged into a 12 m long, 10 m wide, and 2 m deep ocean

basin, as shown in Figure 21(a), and the tunnel was supported at its ends by a steel frame to simulate a hinge connection, as shown in Figure 21(b).

Stainless steel wires of 0.5 mm diameter were used as mooring cables, and a total of 14 mooring cables were spaced equally at 1 m intervals along the longitudinal direction of the tunnel, as shown in Figure 21(b). For each mooring cable, one end was connected to the tunnel using metal ring buckles and the other end was connected to the pad eye welded to a steel frame. The steel frame was fixed at the bottom of the 3D ocean basin using anchor bolts.

Five triaxial MEMS accelerometers, shown in Figure 21(c), were attached at locations 3–7, and 18 resistance-type strain gauges, shown in Figure 21(d), were attached at locations 1, 2, 4, 6, 8, and 9. Three strain gauges were installed at each cross-section at locations 1, 2, 4, 6, 8, and 9 for bidirectional displacement estimation. Note that all strain gauges and accelerometers were installed on the external surface of the SFT mock-up structure, and waterproofed. Fourteen load cells were adopted for all the mooring cables to measure the reference tension forces. All acceleration, strain, and load cell data were sampled at 100 Hz using National Instruments data acquisition devices. Table 1 lists the detailed specifications of these sensors.
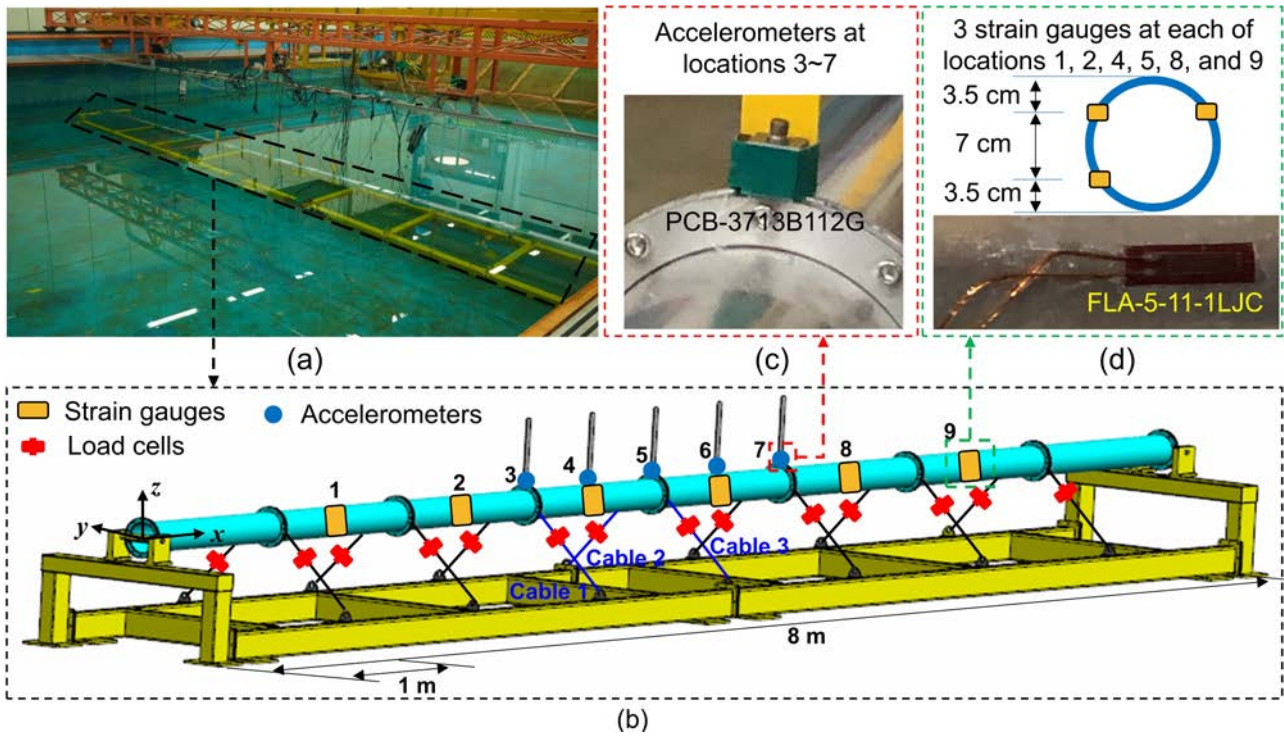
Figure 21. Configuration of the 8 m long aluminum SFT mock-up test: (a) an SFT mock-up structure installed at a 3D ocean basin, (b) overview of the SFT mock-up structure and sensor locations, (c) a triaxial MEMS accelerometer installed at each of the locations 3–7, and (d) three resistance-type strain gauges installed at each cross-section of locations 1, 2, 4, 6, 8 and 9.

After sensor installation, water was poured into the 3D ocean basin to ensure that the SFT mock-up structure was immersed and floating. By adjusting the length of the mooring cables, the initial tension

forces were set to approximately 150 N. Attempts were made to excite the test structure using different wave loadings, but no meaningful vibration was observed owing to the relatively high stiffness of the SFT mock-up structure. Subsequently, the SFT mock-up structure was excited by manually pushing and releasing the tunnel along three different directions: (1) horizontal (y), (2) vertical (z), and (3) inclined, to generate millimeter-level displacements. Under inclined excitation, displacement was generated in both horizontal and vertical directions. Special attention was paid to minimizing the displacement in the longitudinal (x) direction. Owing to the limited data acquisition channels, only the load cells of cables 1, 2, and 3 (as shown in Figure 21(b)) were used to measure the reference tension forces during the three excitations, whereas the other 11 load cells were used only to adjust the initial tension forces.

Table 1. Detailed specifications of accelerometer, strain gauge and load cells used in the 8 m long SFT mock-up test

Sensors	Parameters	Values
Accelerometers (PCB Piezotronics 3713B112G)	Bandwidth	DC - 250Hz
	Full-scale range	± 2g
	Operating temperature	-54 ~ 121 °C
	Sensitivity	1,000 mV/g
	Spectral noise	22.9 μg /$\sqrt{\text{Hz}}$
	Linearity	<1%
Strain gauges (TML FLA-5-11-1LJC)	Grid material	Cu-Ni alloy
	Gauge factor	2.10$\pm$1%
	Gauge resistance	120$\pm$0.5Ω
	Operating temperature	-20 ~ 80 °C
	Transverse sensitivity	-0.5%
Load cells (CASSCALE SMNT-13b)	Non-linearity	1%
	Zero-balance	$\pm$2%
	Repeatability	1%
	Input/output impedance	350$\pm$3Ω
	Operating temperature	-20 ~ 80 °C
	Ultimate load limit	200%

5.2 Reference displacement measurement using computer vision

Computer vision was adopted in this experiment to measure the reference (ground-truth) displacement. Because the tunnel was submerged during the experiment, it was difficult to directly measure its displacement. Instead, five 20 cm long rigid steel bars with two artificial markers, as shown in Figure 22 were attached vertically to the top surface of the tunnel at locations 3–7. Because the tunnel may be subjected to torsion along the x axis, two markers were necessary. Five digital cameras (Sony DSC-WX800) were installed at stationary locations to individually track the movement of the

20

markers at each location. Table 2 presents the detailed specifications of the camera. In this test, each camera recorded the movement of two markers at each location with a 1920×1080 resolution and 119.88 Hz sampling rate. The distance between the cameras and markers varied from 4 m to 7 m. The water level was always below these markers during the experiments to ensure successful tracking of the markers. A commonly used template-matching algorithm [8] was adopted for marker tracking。 Because the original displacement estimated from the vision measurement is in pixel units, a scale factor is required to convert the pixel unit to a length unit. By adjusting the focal length of each camera, a scale factor of 0.1 mm/pixel was achieved for all targets.
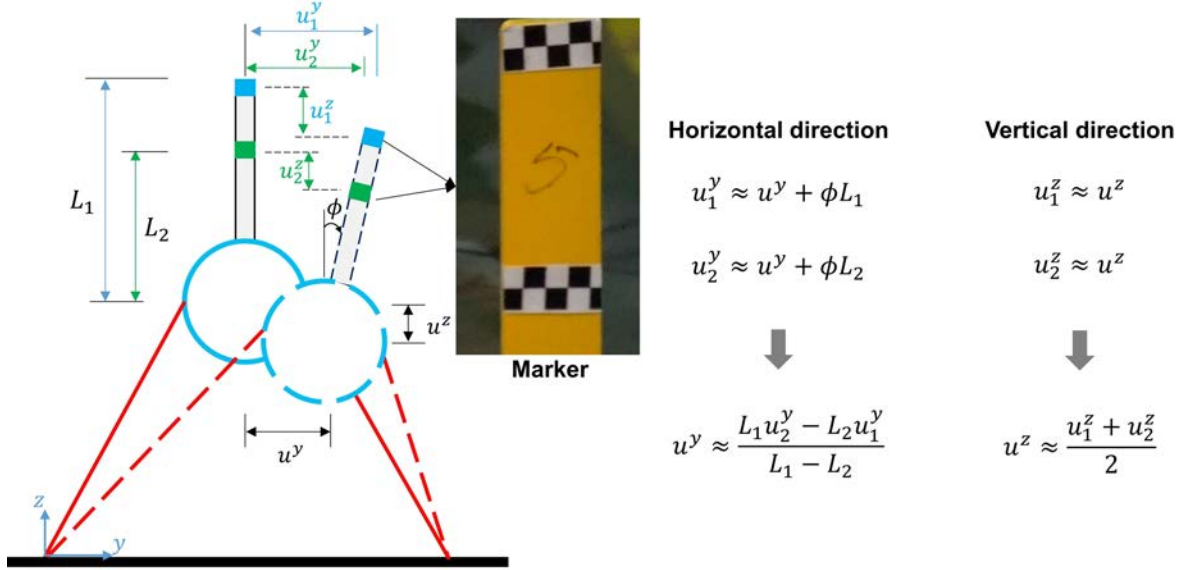

Figure 22. Vision-based reference displacement measurement using two artificial markers at different heights of the rigid steel bar attached to the tunnel.

The reference displacement was computed as the weighted average of the displacements of the two markers, as shown in Figure 22.

$$u^y = \frac{L_1}{L_1 - L_2} u_1^y - \frac{L_2}{L_1 - L_2} u_2^y; \; u^z = \frac{u_1^z + u_2^z}{2} \tag{15}$$

where L_1 and L_2 denote the vertical distances between each marker and tunnel cross-section center, respectively. u_1^y and u_1^z denote the horizontal and vertical displacements of Marker 1, respectively. u_2^y and u_2^z are defined in a similar manner. Because the strain and acceleration measurements were sampled at 100 Hz, the vision-based displacements, which were originally sampled at 119.88 Hz, were down-sampled to 100 Hz.

Table 2. Detailed specifications of digital camera (Sony DSC-WX800)

Parameters	Values
Sensor type	1/2.3 type CMOS sensor
Number of pixels	Approximately 18.2 megapixels
Lens type	Zeiss vario-sonnar lens

Focal length	4.25~118 mm
Optical zoom	28x
Resolution and sampling rate for video recording	1080P (1920×1080) at up to 120 Hz 4K (3840×2160) at up to 30 Hz

5.3 Displacement and tension force estimation results

5.3.1 Displacements

Figure 23 shows the frequency spectra of the acceleration measured at location 3 under an inclined excitation. The contribution of the first mode to the structural displacement was dominant in both the horizontal and vertical directions. Hence, the mode-scaling factors were estimated only for the first mode ($P = 1$) in both directions. The first resonance frequencies of the SFT mock-up structure were observed at 5.16 Hz and 8.02 Hz in the vertical and horizontal directions, respectively.
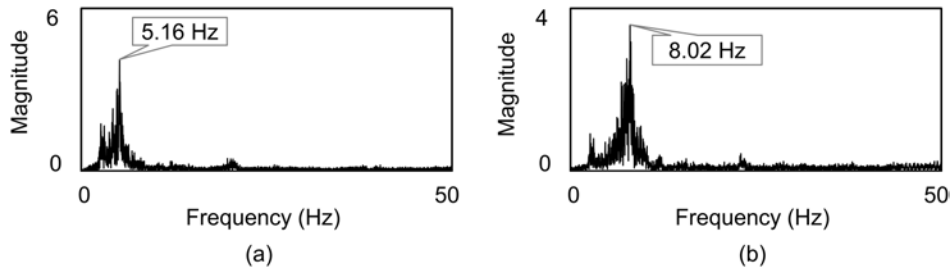

Figure 23. Frequency spectra of (a) vertical and (b) horizontal accelerations measured under the inclined excitation at location 3 of the 8 m long SFT mock-up structure.
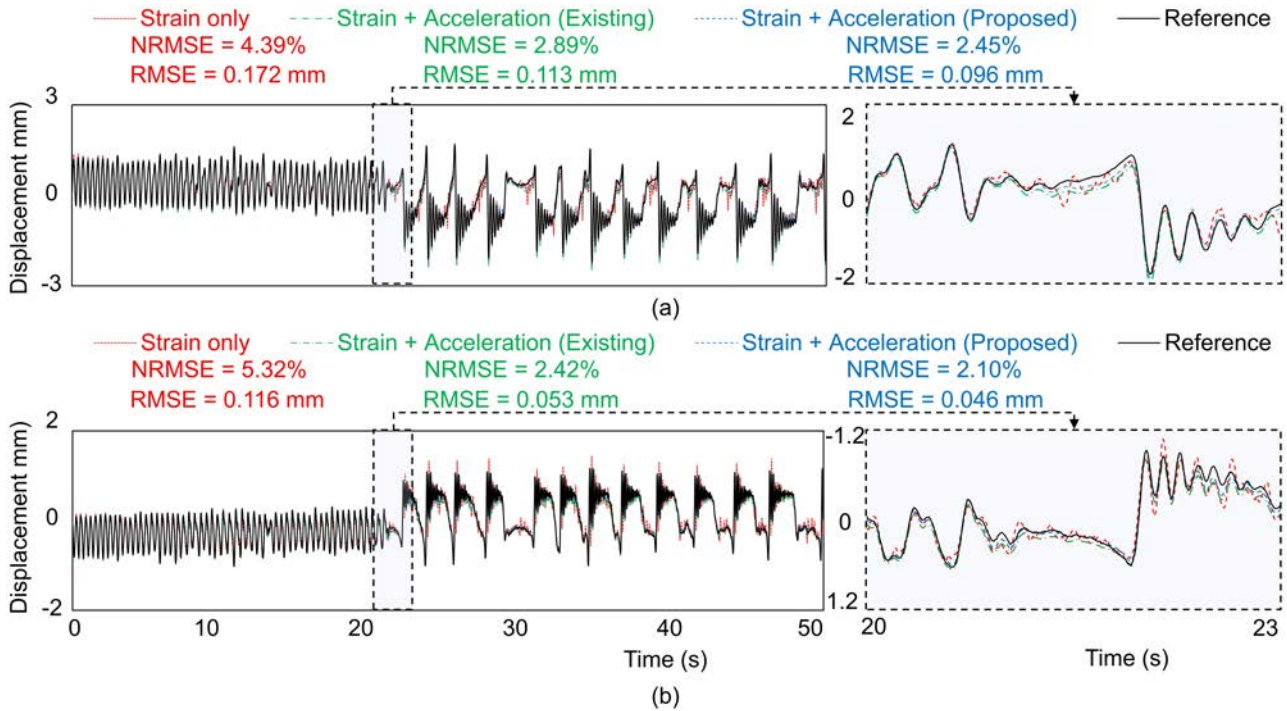

Figure 24. Comparison of (a) vertical and (b) horizontal displacements estimated at location 3 of the aluminum SFT mock-up structure under inclined excitation.

The displacements were estimated at locations 3–7. Figure 24 shows the bidirectional displacements estimated at location 3 under an inclined excitation. Here, displacements were estimated from (1) strain measurement only, (2) the combination of strain and acceleration measurements using the existing technique, and (3) the combination of strain and acceleration measurements using the proposed technique. Significantly larger errors were observed for the strain-based displacements, demonstrating the necessity of combining strain and acceleration measurements. The proposed technique estimated displacements with 2.45% and 2.10% NRMSEs in vertical and horizontal directions, respectively. The RMSEs of the estimated displacements were 0.096 and 0.046 mm in the vertical and horizontal directions, respectively. Compared with the existing technique, approximately 15% error reduction was achieved using the proposed technique, as shown in Figure 24. Note that the proposed technique computes different scaling factors for each mode; however, the scaling factor for a specific mode is constant for different displacement estimation locations. In contrast, the existing technique computes a single scaling factor for all modes, and the scaling factor value varies at each displacement estimation location. However, this did not lead to a significant difference in the displacement estimation in this experiment. Because the contribution of the first mode was significantly more dominant than that of any other mode, only a slight improvement was achieved using the proposed technique.

Table 3. Displacement estimation results obtained from 8 m long SFT mock-up structure test

Excitations (Displacement direction)	Estimation locations	Strain only		Existing technique (strain + acceleration)		Proposed technique (strain + acceleration)	
		RMSE (mm)	NRMSE (%)	RMSE (mm)	NRMSE (%)	RMSE (mm)	NRMSE (%)
Vertical excitation (Vertical)	3	0.058	1.88	0.058	1.86	0.047	1.50
	4	0.091	2.43	0.072	1.92	0.060	1.61
	5	0.072	1.71	0.062	1.46	0.051	1.20
	6	0.077	1.74	0.067	1.52	0.056	1.27
	7	0.120	2.60	0.125	2.70	0.103	2.22
Horizontal excitation (Horizontal)	3	0.079	2.57	0.070	2.29	0.061	1.99
	4	0.094	2.60	0.093	2.54	0.080	2.20
	5	0.101	2.51	0.105	2.60	0.087	2.15
	6	0.134	3.20	0.103	2.45	0.089	2.11
	7	0.156	3.81	0.117	2.86	0.094	2.30
Inclined excitation (Vertical)	3	0.172	4.39	0.113	2.89	0.096	2.45
	4	0.198	3.61	0.128	2.34	0.105	1.92
	5	0.220	3.63	0.136	2.23	0.116	1.91
	6	0.258	3.95	0.159	2.42	0.135	2.06
	7	0.275	4.18	0.168	2.55	0.136	2.06
Inclined excitation (Horizontal)	3	0.116	5.32	0.056	2.55	0.046	2.10
	4	0.092	2.99	0.043	1.40	0.036	1.18
	5	0.100	3.08	0.061	1.89	0.050	1.55

6	0.119	3.72	0.078	2.42	0.065	2.02
7	0.170	5.21	0.147	4.54	0.122	3.76
Average	0.135	3.26	0.098	2.37	0.082	1.98

The displacement estimation performance at all five locations is summarized in Table 3. The overall RMSE and NRMSE of the strain-based displacement were 0.135 mm and 3.26%, respectively. Note that the estimation of strain-based displacement requires mode-scaling factors. Therefore, accelerometers were still required. Combining the acceleration measurements resulted in a significant improvement in displacement estimation accuracy, and around 27% and 40% reductions were obtained by the existing and proposed techniques, respectively, in both RMSE and NRMSEs.
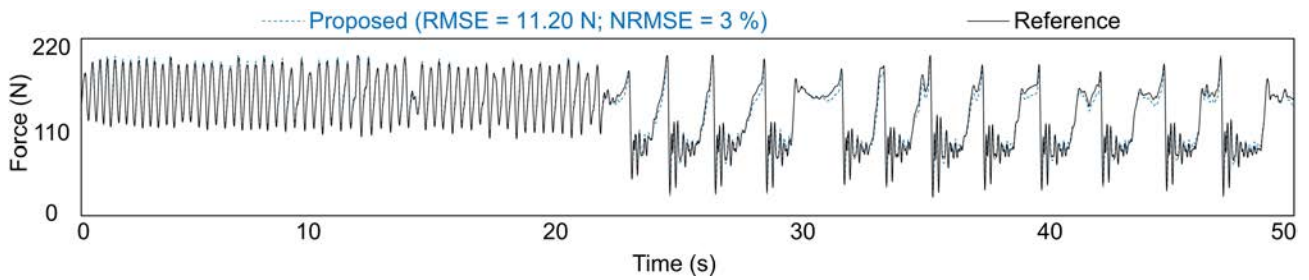
5.3.2 Tension forces

Figure 25. Comparison of the tension force of cable 3 estimated by the proposed technique and measured by a load cell under inclined excitation in the 8 m long SFT mock-up structure test.

The displacements obtained at location 3 were used to estimate the tension force of cable 1, and those from location 5 were used to estimate the tension forces at cables 2 and 3. Figure 25 presents the tension force of cable 3 under inclined excitation. A good agreement between the estimated and reference tension forces was observed with 11.20 NRMSE and 3% NRMSE. The tension forces estimated for all the cases are summarized in Figure 26. The proposed technique successfully estimated the tension forces, and RMSE and NRMSE values were less than 12 N and 4.6%, respectively. It should be noted that the load cells installed on cables 1 and 2 leaked after horizontal excitation, resulting in the failure of the reference tension force measurement under inclined excitation. Therefore, the corresponding NRMSE values were not calculated.
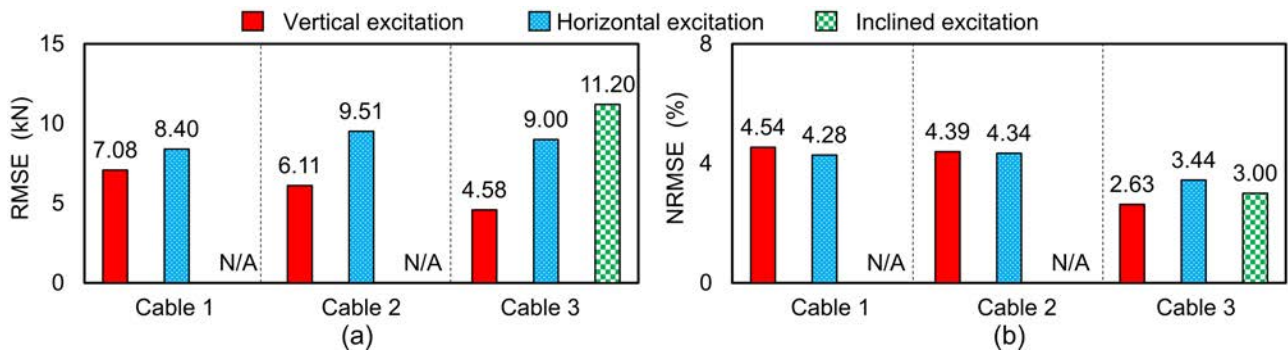

Figure 26. Cable tension force estimation error obtained from 8 m long SFT mock-up structure test

6. Conclusions

This study proposes a simultaneous displacement and cable force estimation technique for SFTs using acceleration and strain measurements. The main contribution of this study lies in the derivation of the strain-displacement transformation relationship for SFTs with simplified mode shapes, automatic mode-scaling factor estimation, and displacement-based mooring cable tension force estimation. The feasibility of the proposed technique was first examined on a numerical SFT model by estimating the bidirectional displacements at thirty-one locations and tension forces at 30 mooring cables. The NRMSE values of the displacements and tension forces estimated using the proposed technique were less than 1% and 2%, respectively. Experimental validation was conducted on an 8 m long aluminum SFT mock-up structure. The overall RMSE and NRMSE values of the estimated displacements were 0.082 mm and 1.98%, respectively. In addition, tension forces of three mooring cables were estimated with RMSE and NRMSE values less than 12 N and 4.6%, respectively. The validation tests performed showed that the proposed technique can compensate for the discrepancy between the true and simplified mode shapes at most locations, and then accurately estimate the SFT displacements. However, it may not work well near the two ends of the tunnel, particularly when the boundary conditions are not symmetric. In addition, in the laboratory test, the SFT mock-up structure was excited by manually pushing and releasing the tunnel due to the its relatively large stiffness. Further studies may be needed to examine the proposed technique under more realistic loading, such as vehicle and wave loading. In such a case, a longer SFT structure with less stiffness than the one investigated in this study is required to generate meaningful vibration.

Declaration of conflicting interests

The authors declared no potential conflicts of interest with respect to the research, authorship, and/or publication of this article.

Data availability statement

The data supporting the findings of the study are available from the corresponding author upon reasonable request

Reference

1. Østlid H. When is SFT competitive? *Procedia Engineering* 2010; **4**: 3–11. DOI: 10.1016/j.proeng.2010.08.003.

2. Shekari MR, Amiri SM, Zareifard MR. A numerical approach for coupled analysis of the seismic response of a cable-moored submerged floating tunnel. *Marine Structures* 2022; **83**: 103156. DOI: 10.1016/j.marstruc.2021.103156.

3. Zou PX, Bricker JD, Chen LZ, Uijttewaal WSJ, Simao Ferreira C. Response of a submerged floating tunnel subject to flow-induced vibration. *Engineering Structures* 2022; **253**: 113809. DOI: 10.1016/j.engstruct.2021.113809.

4. Kim GJ, Kwak HG, Jin C, Kang H, Chung W. Three-dimensional equivalent static analysis for design of submerged floating tunnel. *Marine Structures* 2021; **80**: 103080. DOI: 10.1016/j.marstruc.2021.103080.

5. Won D, Park WS, Kang YJ, Kim S. Dynamic behavior of the submerged floating tunnel moored by inclined tethers attached to fixed towers. *Ocean Engineering* 2021; **237**: 109663. DOI: 10.1016/j.oceaneng.2021.109663.

6. Santhosh KV, Roy BK. Online implementation of an adaptive calibration technique for displacement measurement using LVDT. *Applied Soft Computing* 2017; **53**: 19–26. DOI: https://doi.org/10.1016/j.asoc.2016.12.032.

7. Nickitopoulou A, Protopsalti K, Stiros S. Monitoring dynamic and quasi-static deformations of large flexible engineering structures with GPS: Accuracy, limitations and promises. *Engineering Structures* 2006; **28**(10): 1471–1482. DOI: 10.1016/j.engstruct.2006.02.001.

8. Xu Y, Brownjohn J, Kong D. A non-contact vision-based system for multipoint displacement monitoring in a cable-stayed footbridge. *Structural Control & Health Monitoring* 2018; **25**(5). DOI: 10.1002/stc.2155.

9. Gentile C, Bernardini G. An interferometric radar for non-contact measurement of deflections on civil engineering structures: laboratory and full-scale tests. *Structure and Infrastructure Engineering* 2010; **6**(5): 521–534. DOI: https://doi.org/10.1080/15732470903068557.

10. Guan S, Rice JA, Li C, Li Y, Wang G. Structural displacement measurements using DC coupled radar with active transponder. *Structural Control & Health Monitoring* 2017; **24**(4): e1909.

11. Lee HS, Hong YH, Park HW. Design of an FIR filter for the displacement reconstruction using measured acceleration in low-frequency dominant structures. *International Journal for Numerical Methods in Engineering* 2010; **82**(4): 403–434. DOI: 10.1002/nme.2769.

12. Shin S, Lee SU, Kim Y, Kim NS. Estimation of bridge displacement responses using FBG sensors and theoretical mode shapes. *Structural Engineering and Mechanics* 2012; **42**(2): 229–245. DOI: https://doi.org/10.12989/sem.2012.42.2.229.

13. Helmi K, Taylor T, Zarafshan A, Ansari F. Reference free method for real time monitoring of bridge deflections. *Engineering Structures* 2015; **103**: 116–124. DOI: 10.1016/j.engstruct.2015.09.002.

14. Moschas F, Stiros S. Measurement of the dynamic displacements and of the modal frequencies of a short-span pedestrian bridge using GPS and an accelerometer. *Engineering Structures* 2011; **33**(1): 10–17. DOI: 10.1016/j.engstruct.2010.09.013.

15. Park JW, Sim SH, Jung HJ. Displacement Estimation Using Multimetric Data Fusion. *IEEE-ASME Transactions on Mechatronics* 2013; **18**(6): 1675–1682. DOI: 10.1109/TMECH.2013.2275187.

16. Ma Z, Chung J, Liu P, Sohn H. Bridge displacement estimation by fusing accelerometer and strain gauge measurements. *Structural Control & Health Monitoring* 2021; **28**(8): e2733. DOI: https://doi.org/10.1002/stc.2733.

17. Ma Z, Choi J, Sohn H. Real-time structural displacement estimation by fusing asynchronous acceleration and computer vision measurements. *Computer-Aided Civil and Infrastructure Engineering* 2022; **37**(6): 688–703. DOI: 10.1111/mice.12767.

18. Ma Z, Choi J, Liu P, Sohn H. Structural displacement estimation by fusing vision camera and accelerometer using hybrid computer vision algorithm and adaptive multi-rate Kalman filter. *Automation in Construction* 2022; **140**: 104338. DOI: 10.1016/j.autcon.2022.104338.

19. Ma Z, Choi J, Yang L, Sohn H. Structural displacement estimation using accelerometer and FMCW millimeter wave radar. *Mechanical Systems and Signal Processing* 2023; **182**: 109582. DOI: 10.1016/j.ymssp.2022.109582.

20. Kaur N, Goyal S, Anand K, Sahu GK. A cost-effective approach for assessment of pre-stressing force in bridges using piezoelectric transducers. *Measurement* 2021; **168**: 108324. DOI: 10.1016/j.measurement.2020.108324.

21. Nazarian E, Ansari F, Zhang X, Taylor T. Detection of Tension Loss in Cables of Cable-Stayed Bridges by Distributed Monitoring of Bridge Deck Strains. *Journal of Structural Engineering* 2016; **142**(6): 04016018. DOI: 10.1061/(ASCE)ST.1943-541X.0001463.

22. Feltrin G, Meyer J, Bischoff R, Saukh O. A wireless sensor network for force monitoring of cable stays. *Proceedings of the 3nd International Conference on Bridge Maintenance, Safety and Management, IABMAS*, 2006.

23. Geier R, De Roeck G, Flesch R. Accurate cable force determination using ambient vibration measurements. *Structure and Infrastructure Engineering* 2006; **2**(1): 43–52. DOI: 10.1080/15732470500253123.

24. Yim J, Wang ML, Shin SW, Yun CB, Jung HJ, Kim JT, *et al.* Field application of elasto-magnetic stress sensors for monitoring of cable tension force in cable-stayed bridges. *Smart Structures and Systems* 2013; **12**(3): 465–482. DOI: https://doi.org/10.12989/sss.2013.12.3_4.465.

25. Cappello C, Zonta D, Ait Laasri H, Glisic B, Wang M. Calibration of Elasto-Magnetic Sensors on In-Service Cable-Stayed Bridges for Stress Monitoring. *Sensors* 2018; **18**(2): 466. DOI: 10.3390/s18020466.

26. Kim JM, Lee J, Sohn H. Automatic measurement and warning of tension force reduction in a PT tendon using eddy current sensing. *NDT & E International* 2017; **87**: 93–99. DOI: https://doi.org/10.1016/j.ndteint.2017.02.002.

27. Ma Z, Choi J, Sohn H. Noncontact cable tension force estimation using an integrated vision and inertial measurement system. *Measurement* 2022; **199**: 111532. DOI: 10.1016/j.measurement.2022.111532.

28. Feng D, Scarangello T, Feng MQ, Ye Q. Cable tension force estimate using novel noncontact vision-based sensor. *Measurement* 2017; **99**: 44–52. DOI: https://doi.org/10.1016/j.measurement.2016.12.020.

29. Sato M, Kanie S, Mikami T. Mathematical analogy of a beam on elastic supports as a beam on elastic foundation. *Applied Mathematical Modelling* 2008; **32**(5): 688–699. DOI: 10.1016/j.apm.2007.02.002.

30. Mirzapour J, Shahmardani M, Tariverdilo S. Seismic response of submerged floating tunnel under support excitation. *Ships and Offshore Structures* 2017; **12**(3): 404–411. DOI: 10.1080/17445302.2016.1171591.

31. Xiang Y, Yang Y. Spatial dynamic response of submerged floating tunnel under impact load. *Marine Structures* 2017; **53**: 20–31. DOI: 10.1016/j.marstruc.2016.12.009.

32. Lin H, Xiang Y, Yang Y, Chen Z. Dynamic response analysis for submerged floating tunnel due to fluid-vehicle-tunnel interaction. *Ocean Engineering* 2018; **166**: 290–301. DOI: 10.1016/j.oceaneng.2018.08.023.

33. Jin C, Chung WC, Kwon DS, Kim M. Optimization of tuned mass damper for seismic control of submerged floating tunnel. *Engineering Structures* 2021; **241**: 112460. DOI: 10.1016/j.engstruct.2021.112460.

34. Jin C, Bakti FP, Kim M. Time-domain coupled dynamic simulation for SFT-mooring-train interaction in waves and earthquakes. *Marine Structures* 2021; **75**: 102883. DOI: 10.1016/j.marstruc.2020.102883.

35. Jin C, Kim MH. Tunnel-mooring-train coupled dynamic analysis for submerged floating tunnel under wave excitations. *Applied Ocean Research* 2020; **94**: 102008. DOI: 10.1016/j.apor.2019.102008.

36. Xiang Y, Chen Z, Yang Y, Lin H, Zhu S. Dynamic response analysis for submerged floating tunnel with anchor-cables subjected to sudden cable breakage. *Marine Structures* 2018; **59**: 179–191.

37. Jeong K, Min S, Jang M, Won D, Kim S. Feasibility study of submerged floating tunnels with vertical and inclined combined tethers. *Ocean Engineering* 2022; **265**: 112587. DOI: 10.1016/j.oceaneng.2022.112587.

38. Won D, Kim S. Feasibility Study of Submerged Floating Tunnels Moored by an Inclined Tendon System. *International Journal of Steel Structures* 2018; **18**(4): 1191–1199. DOI: 10.1007/s13296-018-0102-2.

39. Chen L, Basu B, Martin CI. On rotational flows with discontinuous vorticity beneath steady water waves near stagnation. *Journal of Fluid Mechanics* 2021; **912**: A44. DOI: 10.1017/jfm.2020.1057.

40. Remseth S, Leira BJ, Okstad KM, Mathisen KM, Haukås T. Dynamic response and fluid/structure interaction of submerged floating tunnels. *Computers & Structures* 1999; **72**(4): 659–685. DOI: 10.1016/S0045-7949(98)00329-0.

41. Hong YH, Lee SG, Lee HS. Design of the FEM-FIR filter for displacement reconstruction using accelerations and displacements measured at different sampling rates. *Mechanical Systems and Signal Processing* 2013; **38**(2): 460–481. DOI: https://doi.org/10.1016/j.ymssp.2013.02.007.

Appendix: Introduction to FIR filter-based displacement estimation

An FIR filter-based technique was used to estimate displacement from acceleration [11] and then extended to combine the acceleration and initial displacement measured by an LVDT [41] or estimated by strain gauges [16] for final displacement estimation. The final displacement had a higher accuracy than the initial displacement. The working principle of the FIR-based technique is briefly described as follows.

Provided that the acceleration measurement ($\boldsymbol{a}$) and initial displacement estimation or measurement ($\boldsymbol{u}$) are available within a given time window $[(k - M)\Delta t, (k + M)\Delta t]$,

$$\boldsymbol{a} = [a_{k-M+1}, a_{k-M+2}, \cdots, a_{k+M-1}]^T; \quad \boldsymbol{u} = [u_{k-M}, u_{k-M+1}, \cdots, u_{k+M}]^T \tag{A1}$$

An error function $\Pi\{\widehat{\boldsymbol{u}}\}$ is defined for the final displacement ($\widehat{\boldsymbol{u}}$), as follows:

$$\Pi(\widehat{\boldsymbol{u}}) = \frac{1}{2}\|\boldsymbol{L}_a\boldsymbol{L}_c\widehat{\boldsymbol{u}} - \boldsymbol{L}_a(\Delta t)^2\boldsymbol{a}\|_2^2 + \frac{\lambda^2}{2}\|\widehat{\boldsymbol{u}} - \boldsymbol{u}\|_2^2; \quad \widehat{\boldsymbol{u}} = [\hat{u}_{k-M}, \hat{u}_{k-M+1}, \cdots, \hat{u}_{k+M}]^T \tag{A2}$$

where $\boldsymbol{L}_a$ and $\boldsymbol{L}_c$ denote the weighting matrix and second-order differential operator matrix, respectively, $\|\cdot\|_2$ denotes the two-norm of a vector, Δt denotes the time interval of measurements, λ is the regularization factor defined as

$$\lambda = 46.81(\frac{2.68}{f_1\Delta t})^{-1.95} \tag{A3}$$

where f_1 is the first resonance frequency of the target structure where displacement is to be estimated. More details can be found in Lee et al. [11].

By minimizing $\Pi\{\widehat{\boldsymbol{u}}\}$ with respect to $\widehat{\boldsymbol{u}}$, $\widehat{\boldsymbol{u}}$ can be estimated as,

$$\hat{\boldsymbol{u}} = (\Delta t)^2 \left(\boldsymbol{L}^T \boldsymbol{L} + \lambda^2 \boldsymbol{I}\right)^{-1} \boldsymbol{L}^T \boldsymbol{L}_a \boldsymbol{a} + \lambda^2 \left(\boldsymbol{L}^T \boldsymbol{L} + \lambda^2 \boldsymbol{I}\right)^{-1} \boldsymbol{u}; \ \boldsymbol{L} = \boldsymbol{L}_a \boldsymbol{L}_c \tag{A4}$$

Because the highest estimation accuracy is achieved at the center of the time window $[(k - M)\Delta t, (k + M)\Delta t]$, only the displacement estimated at the center was retained.

$$\hat{u}_k = \boldsymbol{C}_H \boldsymbol{a} + \boldsymbol{C}_L \boldsymbol{u} \tag{A5}$$

where $\boldsymbol{C}_H$ and $\boldsymbol{C}_L$ denote the $(N + 1)^{th}$ row of $\{(\Delta t)^2 (\boldsymbol{L}^T \boldsymbol{L} + \lambda^2 \boldsymbol{I})^{-1} \boldsymbol{L}^T \boldsymbol{L}_a\}$ and $\{\lambda^2 (\boldsymbol{L}^T \boldsymbol{L} + \lambda^2 \boldsymbol{I})^{-1}\}$, respectively.